École polytechnique de Louvain

Sensitivity analysis on the operational parameters affecting combustion markers in MILD regime

Author: **Adrien Allard**
Supervisors: **Francesco Contino, Pietro Pagani**
Reader: **Miltiadis Papalexandris**

Academic year 2020–2021
Master [120] in Mechanical Engineering

Acknowledgements

Foremost, I would like to express my appreciation to my thesis supervisor, Pr. F. Contino, for his support, guidance and availability, specially in crucial moments. My gratitude goes also to PhD. P. Pagani, for his involvement as a mentor with its numerous advices but also his help on the simulation debugging.

My thanks go also to Pr. M. Papalexandris, for his participation in the evaluation of the present work.

The simulations, basis of this study, were possible thanks to the supercomputing utility, namely the Consortium des Équipements de Calcul Intensif en Fédération Wallonie Bruxelles (CÉCI) funded by the Fond de la Recherche Scientifique de Belgique (F.R.S.-FNRS).

I would also express my deepest thanks to my parents. Their support of all kinds brought an important contribution in the writing of this master thesis. Thank you.

Finally, I thank the rest of my family and friends whom, in a way or another, also contributed to this achievement.

Contents

List of Figures

List of Tables

Chapter 1

Introduction

The improvement of energy efficiency in the power generation sector is among the actions taken by the European Union to meet its emissions reduction target[1]. It is in this perspective, together with a strong will to be an important actor in the low-carbon economy, that the NextMGT research program emerged. It involves the development of micro gas turbines (MGT) to make them reach their full potential, which is currently not the case due to a lack of investment[2]. This technology presents interesting features when considering a shift towards sustainable energy production: high efficiency can be achieved while offering a fuel flexibility and less maintenance than full-scale gas turbines.

One aspect of the program concerns the investigation on the combustion technology that could ensure low pollutant emissions while fulfilling the above requirements[2]. Moderate or Intense Low oxygen Dilution (MILD) combustion appears as a good candidate. This regime lies in the recirculation of hot exhaust gases to preheat the reactant mixture above its auto-ignition temperature, which allows to get rid of an activator to start the combustion (e.g. a spark). Moreover, MILD most interesting feature is its capacity to emit ultra-low NOx[3]. On the other hand, Colorado et al.[4] have shown that the same magnitude order of thermal efficiency could be reached for the combustion of natural gas or biogas. However, a Damköhler number of 1 characterises the regime. It complicates the research and development of the technology such as no aggregated definition of the conditions to achieve MILD combustion currently exists[3].

The present chapter first covers a literature review of the MILD regime and exposes its challenges. Then, the concept of Uncertainty Quantification is introduced whose utility is underlined in the last section with the objectives and the structure of this work.

1.1 Moderate or Intense Low oxygen Dilution combustion

MILD combustion is visually characterised by an almost homogeneous reaction zone with a hardly visible flame, which is worth its other name of flameless combustion. This homogeneity results from a high recirculation rate of exhaust gases (EGR or coflow)[5]. With their hot temperature, they preheat the reactants. The fuel reaches its self-ignition temperature (T_{ign}) which makes it react spontaneously with the preheated oxidiser. It allows to reduce the temperature rise ΔT between the reactants T_r and the products T_p such as $\Delta T = T_p - T_r < T_{ign}$ is believed to be a condition of MILD combustion[3]. This smaller ΔT yields to a more stable and distributed combustion[6]. The dilution induced by the exhaust gases also reduces the maximal temperature due to their high specific heat capacities. The NOx production mainly driven by the temperature is therefore impacted. Moreover, the almost homogeneous reaction zone limits the apparition of hot spots and the lean environment reduces the availability of NOx main reactant: the oxygen. Indeed, the concentration of this latter varies between 3% to 15% with regards to the burner type[3].

Experimental burners were developed to study MILD combustion. The famous ones are the Adelaide and Delft Jet in Hot Coflow (AJHC and DJHC respectively). The objective of these latter is to capture the physical process behind flameless combustion rather than for optimisation. It is the reason why the vitiated coflow is achieved through secondary burners instead of a recuperative system[7]. The two burners are similar but the difference lies in their coflow cooling technique. Where the AJHC uses additional N_2 as dilutant, the DJHC does it through heat losses (both radiative and convective) all along the burner.
Unfortunately, the usual scaling between laboratory and industrial burners can not be considered anymore[8]. Therefore, the modelisation of the regime through Computational Fluid Dynamics (CFD) would allow to optimise the geometry as well as to better understand the phenomenology at lower costs. However, the high dilution and lower temperatures slow down the reactions rate while the turbulence is enhanced by high EGR. It makes the chemistry and turbulent time scales (τ_C, τ_T respectively) comparable which gives a Damköhler number ($Da = \frac{\tau_T}{\tau_C}$) around one in the reaction zone [8][3]. Consequently, MILD combustion is driven as much by the chemical reactions than by the fluid dynamics. It hinders considerably the development of a CFD model as it requires to use both turbulence model and accurate finite rate approach for chemistry.

1.2 Uncertainty Quantification

The increasing complexity of engineering systems led the Uncertainty Quantification (UQ) to become a field of interest in modelling. It aims at determining how likely outcomes of a system vary with stochastic inputs (also known as uncertainties) which better represent real-life applications[9]. Other sources of uncertainties can lie in assumptions of numerical models, governing equations or the case geometry. Therefore, stochastic CFD simulations appear as a solid foundation towards the acquisition of more robust simulations[10].

To propagate the uncertainties in the system, there exists intrusive and non-intrusive methods. When dealing with complex models, the non-intrusive approach is generally preferred as it requires no other modification of the code than inputs value[10]. The Polynomial Chaos Expansion (PCE) sampling-based method is one of them. It decomposes the system into a series of orthogonal polynomials. Then, it computes the corresponding coefficients and builds a dependency model between an output and each uncertainty. Using a regression method, the number of evaluations required to build this model with PCE is less expensive than other method. As example, Monte-Carlo is also a well-known surrogate modelling approach but it can not be considered for computationally demanding simulations. It needs at least 10^3 evaluations to achieve an admissible accuracy[11] and the sparsity of the PCE is generally preferred.

1.3 Scope of the work

Recently, Dr. Z. Li developed an accurate CFD model of MILD combustion. It was achieved considering a simplified version of a DJHC burner and experimental data (non-uniform) were taken as boundary conditions[12]. While MILD combustion is qualitatively expected to provide high combustion efficiency[3], no value of this latter could be found in the literature to the best of the author knowledge. The purpose of the present work is therefore to quantify this efficiency and to determine its main drivers among operational parameters available in the simulation inputs. This way, the results of such study would allow to extend the understanding of the regime and to propose optimisation pathways for current experimental burners.
However, a preliminary evaluation of the combustion efficiency has shown the limits of the simulation. Therefore, other markers of combustion (fuel consumption, maximal temperature, flame width) were developed to cover the phenomenology of the process.

To achieve this objective, the Robust design optimisation of renewable Hydrogen and dErIved energy cArrier systems (RHEIA) framework[13], developed by PhD. D. Coppitters and PhD. P. Tsirikoglou, is used to build the surrogate model of the outputs through a non-intrusive PCE. Yet, it requires to modify some inputs values and their real distribution at the inlets are unknown for a different set-up than the one of the reference simulation. In this case, the best guess is often to consider an uniform distribution. Therefore, the boundary conditions of the simulation needs to be adapted and it represents the first objective of this work.

The present study is divided into 3 parts.
Two sections compose the chapter 2. It consists of a general description of the simulation with its governing equations, models and main algorithm. After ending the first section with the geometry, the second one addresses the modifications applied on the simulation boundary conditions. Follows an analysis on the validity of this simulation with its new configurations.
The chapter 3 is about the set-up of the statistical analysis. At first, a mathematical background on the PCE is provided. Then, the uncertainties are selected with regards to the outputs of interest. This chapter ends with the definition of the stochastic intervals and the tests performed to validate them.
The last part, chapter 4, presents the outcomes of the study with regards to the limitations of the simulation.

Chapter 2

Adaptation of MILD simulation

The chapter is decomposed in two sections.
The first one begins with the description of the Finite Volume Method concept which hides behind a CFD simulation as in the Open Field Operation and Manipulation (OpenFOAM) software. The governing equations of the turbulence and combustion models are then derived. Follow the description of the Tabulation and Adaptive Chemistry approach to speed up the chemistry, and the algorithm solving the equations system. The section ends with the presentation of the case geometry.

The second section describes the work towards a simulation with uniform boundary conditions. The latter is then compared to the reference simulation (with non-uniform boundary conditions) to evaluate its validity for the UQ analysis. An improvement of the temperature prediction by the combustion model ends the section.

2.1 Description of the simulation

2.1.1 Software & Solver

Under the OpenFOAM software, the *reactingFoam* solver is used to solve the flow field equations for a combustion with chemical reactions. The solutions are developed thanks to the Finite Volume Method (section 2.1.2) and a pressure-based iterative process, namely the PIMPLE algorithm (section 2.1.6). An example of an OpenFOAM case structure is provided in Appendix A.
The simulation provided for the present work was developed under an older version of the software than the one available on the CECI cluster. It required the combined forces of Pr. F. Contino and PhD. P. Pagani to make it run on the latest version.

2.1.2 Finite Volume Method

The Finite Volume Method discretises the domain of study into a finite number of cells of convex shapes and planar faces. The partial derivatives equations governing the flow are decomposed into a linear algebraic system. A mean solution of the equations is computed for every cell and is stored at the cell centroid (collocated arrangement)[14], such as for a quantity ζ and a cell with a centre of mass P:

$$\int_{V_P} \zeta(x) dV = \overline{\zeta} \cdot V_P = \zeta_P \cdot V_P \tag{2.1}$$

To illustrate the decomposition methodology, the general transport equation - which is used to derive the Navier-Stokes equations in the next section - is considered. First, the equation is evaluated over the volume of a cell with the previous centre of mass and for the same quantity:

$$\int_{V_P} \frac{\partial}{\partial t}(\rho\zeta)\ dV + \int_{V_P} \nabla \cdot (\rho\zeta u)\ dV = \int_{V_P} \nabla \cdot (\rho\Gamma_\zeta \nabla\zeta)\ dV + \int_{V_P} S_\zeta(\zeta)\ dV \tag{2.2}$$

Then, the volume integral of the convective and diffusive terms are transformed into surface integral thanks to the divergence theorem. The latter states that "*the vector field flux over a closed surface (∂V) is equivalent to the volume integral of the divergence over the region inside the surface*"[14]:

$$\int_{V_P} \nabla \cdot x\ dV = \oint_{\partial V} dS \cdot x \tag{2.3}$$

The Eq. 2.2 becomes:

$$\int_{V_P} \frac{\partial}{\partial t}(\rho\zeta)\ dV + \oint_{\partial V_P} dS \cdot (\rho\zeta u) = \oint_{\partial V_P} dS \cdot (\rho\Gamma_\zeta \nabla\zeta) + \int_{V_P} S_\zeta(\zeta)\ dV \tag{2.4}$$

The convective and diffusive fluxes hence obtained are expressed as a sum of the contribution of each face surface (S_f). Then, the mid-point rule estimates these expressions such as:

$$\sum_f \int_f dS \cdot x_f \ \approx\ \sum_f S_f \cdot x_f \tag{2.5}$$

With the decomposition of the source term into constant and non-linear parts ($S_\zeta(\zeta) = S_C + S_P \cdot \zeta$) and considering the collocated arrangement, Eq. 2.4 becomes:

$$\int_{V_P} \frac{\partial}{\partial t}(\rho\zeta)\; dV + \sum_f S_f \cdot (\rho\zeta u)_f = \sum_f S_f \cdot (\rho\Gamma_\zeta \nabla\zeta)_f + [S_C \cdot V_P + S_P \cdot V_P \cdot \zeta_P] \quad (2.6)$$

After applying spatial and temporal discretisation on every cell, the linear algebraic equations system can be obtained:

$$A \cdot \zeta = b \quad (2.7)$$

With A a matrix of coefficients, ζ and b vectors.
The system is then solved with the iterative procedure, namely the PIMPLE algorithm presented in section 2.1.6. The discretisation schemes (Table 2.1) are specified in the *system/fvSchemes* file. More details on the different schemes can be found in [14][15].

Scheme	Type	Model
Time	Time	localEuleur
Gradient	Spatial	Gauss linear
Divergence	Spatial	Gaus LimitedLinear
Laplacian	Spatial	Gauss linear orthogonal
Interpolation	Spatial	linear
snGradient	Spatial	orthogonal

Table 2.1: Spatial and temporal discretisation schemes.

2.1.3 Turbulence model

Turbulent flows involve irregular temporal and spatial variations in the velocity field. Therefore, by covering the smallest and largest lengths and time scales of the flow, the quantity of information provided by the Navier-Stokes equations has to be decreased through a statistical approach when dealing with high-Reynolds flows[16]. The Reynolds-Averaged Navier-Stokes (RANS) approach models the turbulence in this simulation. The method allows to conduct early stage academic studies with a lower cost compared to Large Eddy Simulation model[17]. In RANS method, the solution of the turbulent flow is obtained through the time-averaging of the Navier-Stokes equations.

It uses the Favre decomposition[1] to dissociate an instantaneous physical quantity into two contributions: a time-averaged part (denoted by the operator: $\tilde{}$) and a fluctuating part (denoted by the operator: "). For example, the instantaneous velocity would be expressed as:

$$u = \tilde{u} + u" \tag{2.8}$$

such as the time averaged part reads:

$$\tilde{u}(t, x, y, z) = \frac{1}{\overline{\rho}\ T} \int_{t-T/2}^{t+T/2} \rho(t', x, y, z)\ u(t', x, y, z)\ dt' \tag{2.9}$$

In the coming demonstrations, and if not precised, when decomposition is mentioned, it is in the Favre sense such as Eq. 2.8. And by *averaging*, it is in the Reynolds sense such as:

$$\overline{u}(t, x, y, z) = \frac{1}{T} \int_{t-T/2}^{t+T/2} u(t', x, y, z)\ dt' \tag{2.10}$$

The operators are submitted to properties that matter for the governing equations derivation. A quantity ζ is taken as example:

$$\overline{\rho\ \zeta"} = 0 \tag{2.11}$$

$$\overline{\rho\ \tilde{\zeta}} = \overline{\rho}\ \tilde{\zeta} \tag{2.12}$$

$$\overline{\rho\ \zeta\ \phi} = \overline{\rho}\ \tilde{\zeta}\ \tilde{\phi} + \overline{\rho}\ \widetilde{\zeta"\ \phi"} \tag{2.13}$$

$$\overline{\rho\ \tilde{\zeta}\phi} = \overline{\rho}\ \tilde{\zeta}\tilde{\phi} \tag{2.14}$$

$$\overline{a \cdot \rho\ \zeta} = a \cdot \overline{\rho}\ \tilde{\zeta} \tag{2.15}$$

$$\overline{\frac{\partial(\rho\ \zeta)}{\partial t}} = \frac{\partial(\overline{\rho}\ \tilde{\zeta})}{\partial t} \tag{2.16}$$

$$\overline{\nabla(\rho\ \zeta)} = \nabla(\overline{\rho}\ \tilde{\zeta}) \tag{2.17}$$

The Navier-Stokes equations can now be derived, the indexed notations are of use.

Mass conservation

The mass conservation equation reads:

$$\frac{\partial \rho}{\partial t} + \frac{\partial}{\partial x_j}(\rho u_j) = 0 \tag{2.18}$$

After the application of the Favre decomposition, the quantities are averaged and with the properties of the operators, it becomes:

$$\frac{\partial \overline{\rho}}{\partial t} + \frac{\partial}{\partial x_j}(\overline{\rho}\ \widetilde{u_j}) = 0 \tag{2.19}$$

[1]The Favre decomposition is applied here instead of the Reynolds one due to high changes in the density during the combustion[18].

Momentum conservation
The momentum conservation equation reads (neglecting external forces):

$$\frac{\partial \rho u_i}{\partial t} + \frac{\partial}{\partial x_j}(\rho u_i u_j) = -\frac{\partial p}{\partial x_i} + \frac{\partial \tau_{ij}}{\partial x_j} \tag{2.20}$$

with τ_{ij} the viscous stress tensor.
The Favre decomposition gives:

$$\frac{\partial \rho(\widetilde{u_i} + u_i")}{\partial t} + \frac{\partial}{\partial x_j}[\rho(\widetilde{u_i} + u_i")(\widetilde{u_j} + u_j")] = -\frac{\partial(\widetilde{p} + p")}{\partial x_i} + \frac{\partial(\widetilde{\tau_{ij}} + \tau_{ij}")}{\partial x_j} \tag{2.21}$$

The averaging and with the operators properties, this expression leads to:

$$\frac{\partial(\overline{\rho}\ \tilde{u}_i)}{\partial t} + \frac{\partial}{\partial x_j}(\overline{\rho}\tilde{u}_i\tilde{u}_j) = -\frac{\partial \widetilde{p}}{\partial x_i} + \frac{\partial}{\partial x_j}(\widetilde{\tau_{ij}} - \overline{\rho}\widetilde{u_i"u_j"}) \tag{2.22}$$

An additional term appears in the equation and it depends on fluctuating quantities. This term is known as the Reynolds stress tensor $\widetilde{\sigma}^t_{ij}$. It implies that the equations cannot be solved directly and the tensor requires a modelisation. This issue is known as the closure problem. It aims at closing and solving the equations in terms of mean flow quantities. An accepted model of the tensor follows the Boussinesq approximation, also known as the eddy viscosity model (EVM). At first, $\widetilde{\sigma}^t_{ij}$ is decomposed into deviatoric and spheric parts:

$$\widetilde{\sigma}^t_{ij} = \widetilde{\tau}^t_{ij} + \frac{1}{3}\widetilde{\sigma}^t_{kk}\delta_{ij} \tag{2.23}$$

with δ_{ij} the Kronecker delta.
The kinetic energy of turbulence fluctuations is expressed as:

$$\tilde{k} = \frac{\widetilde{u_k"u_k"}}{2} = -\frac{\widetilde{\sigma}^t_{kk}}{2\overline{\rho}} \tag{2.24}$$

The EVM states that the deviatoric part of the Reynolds stress tensor is proportional to the deviatoric part of the mean strain-rate tensor:

$$\widetilde{\tau}^t_{ij} = 2\mu_t\widetilde{d}^{dev}_{ij} = 2\mu_t\left(d_{ij} - \frac{1}{3}\frac{\partial\widetilde{u_k}}{\partial x_k}\delta_{ij}\right) \tag{2.25}$$

Therefore, using Eq. 2.24 and 2.42 into Eq. 2.23, the modelisation of the Reynolds stress tensor becomes:

$$\widetilde{\sigma}_{ij}^{t} = -\overline{\rho}\ \widetilde{u_i"u_j"} = \mu_t \left[\left(\frac{\partial \widetilde{u_i}}{\partial x_j} + \frac{\partial \widetilde{u_j}}{\partial x_i} \right) - \frac{2}{3} \frac{\partial \widetilde{u_k}}{\partial x_k} \delta_{ij} \right] - \frac{2}{3} \overline{\rho} \widetilde{k} \delta_{ij} \tag{2.26}$$

The momentum equation becomes then:

$$\frac{\partial(\overline{\rho}\ \tilde{u_i})}{\partial t} + \frac{\partial}{\partial x_j}(\overline{\rho} \tilde{u_i} \tilde{u_j}) = -\frac{\partial \overline{p}}{\partial x_i} + \frac{\partial}{\partial x_j}(\widetilde{\tau_{ij}} - \widetilde{\sigma}_{ij}^{t}) \tag{2.27}$$

The only remaining unknown is the turbulent dynamic eddy viscosity μ_t, which also requires a modelisation. In the k-ϵ model, it is expressed in terms of a constant C_μ, the mean turbulent kinetic energy ($\tilde{k}$) and the mean dissipation rate of k ($\tilde{\epsilon}$):

$$\mu_t = C_\mu \frac{\overline{\rho} \widetilde{k}^2}{\widetilde{\epsilon}} \tag{2.28}$$

$\widetilde{k}$ and $\widetilde{\epsilon}$ are obtained by solving the 2D-system composed of their transport equation, which reads:

$$\frac{\partial(\overline{\rho} \widetilde{k})}{\partial t} + \frac{\partial}{\partial x_j}(\overline{\rho} \tilde{k} \tilde{u_i}) = \frac{\partial}{\partial x_j} \left[\left(\mu + \frac{\mu_t}{\sigma_k} \right) \frac{\partial \widetilde{k}}{\partial x_j} \right] + G_k - \overline{\rho} \widetilde{\epsilon} \tag{2.29}$$

$$\frac{\partial(\overline{\rho} \widetilde{\epsilon})}{\partial t} + \frac{\partial}{\partial x_j}(\overline{\rho} \tilde{\epsilon} \tilde{u_j}) = \frac{\partial}{\partial x_j} \left[\left(\mu + \frac{\mu_t}{\sigma_\epsilon} \right) \frac{\partial \widetilde{\epsilon}}{\partial x_j} \right] + C_{1\epsilon}\ \frac{\widetilde{\epsilon}}{\widetilde{k}} G_k - C_{2\epsilon}\ \overline{\rho} \frac{\widetilde{\epsilon}^2}{\widetilde{k}} \tag{2.30}$$

with the kinetic energy production rate $G_k = -\overline{\rho} \widetilde{u_i"u_j"}\ \frac{\partial \widetilde{u_i}}{\partial x_j}$.
These expressions ensue from both the subtraction of Eq. 2.18 with Eq. 2.19 and Eq. 2.20 with Eq. 2.27. After the decomposition of the instantaneous quantities and the definition of the turbulent kinetic energy (Eq. 2.24), Eq. 2.29 is obtained regarding assumptions and modelisation[19][16]. An analogy of this equation is made to obtain Eq. 2.30.

For the standard k-ϵ model used in this simulation, the coefficients of Eq. 2.28, 2.29 and 2.30 are specified in Table 2.2[20]. There exists other values set of the coefficients but these ones suit well the combustion model used in this simulation[12].

C_μ	$C_{1\epsilon}$	$C_{2\epsilon}$	σ_k	σ_ϵ
0.09	1.44	1.92	1	1.3

Table 2.2: Turbulence model coefficients.

Note that the dynamic viscosity μ is found thanks to the Sutherland transport:

$$\mu = \frac{A_s\sqrt{T}}{1 + \frac{T_s}{T}} \tag{2.31}$$

with A_s and T_s the Sutherland coefficient and temperature, specified for each specie in *chemistry/thermoFile* among the coefficients of Eq. 2.37 and 2.38.

Energy conservation

The energy equation can be derived starting from the transport equation. For a quantity ϕ and using Fick's law for the diffusion term, it reads:

$$\frac{\partial \rho\phi}{\partial t} + \frac{\partial}{\partial x_j}(\rho\phi u_j) = \frac{\partial}{\partial x_j}(\rho\Gamma_\phi \frac{\partial \phi}{\partial x_j}) + S_\phi \tag{2.32}$$

with the diffusion coefficient Γ_ϕ, and S_ϕ a source term.
For the energy, these terms correspond to the thermal diffusivity α and the heat source (from chemical reactions and radiation) respectively. Also, for diffusion (non-premixed) flames, important radiative heat losses q_r can be encountered. Therefore, the energy equation becomes:

$$\frac{\partial \rho h}{\partial t} + \frac{\partial}{\partial x_j}(\rho h u_j) = \frac{\partial}{\partial x_j}(\rho\alpha \frac{\partial h}{\partial x_j}) - \frac{\partial}{\partial x_j}(q_{r,j}) + S_{hc} \tag{2.33}$$

By applying the averaging and with respect to the operators properties, it becomes:

$$\frac{\partial \overline{\rho}\widetilde{h}}{\partial t} + \frac{\partial}{\partial x_j}(\overline{\rho}\widetilde{h}\widetilde{u_j}) = \frac{\partial}{\partial x_j}\left(\overline{\rho}\alpha \frac{\partial \widetilde{h}}{\partial x_j} - \overline{\rho}\widetilde{u_j\text{"}h\text{"}}\right) - \frac{\partial}{\partial x_j}(\overline{q_{r,j}}) + \overline{S}_{hc} \tag{2.34}$$

Here again an additional term depending on a fluctuating quantity appears. This one is known as the effective heat flux. It also requires an approximation such as the Reynolds stress tensor:

$$-\overline{\rho}\widetilde{u_j\text{"}h\text{"}} = \frac{\mu_t}{Pr_t}\frac{\partial \widetilde{h}}{\partial x_j} \tag{2.35}$$

with the turbulent Prandtl number $Pr_t = \frac{\nu_t}{\alpha_t}$ which describes the ratio between the turbulent momentum and thermal diffusivities. Note that $\nu_t = \frac{\mu_t}{\rho}$. μ_t is approximated the same way as in Eq. 2.28.
The enthalpy is expressed as:

$$\widetilde{h} = \sum_{s=1}^{N} \widetilde{Y}_s \widetilde{h}_s \tag{2.36}$$

for N species in the gas mixture and with the mean mass fraction of each specie $\tilde{Y}_s$.

The file *constant/thermophysicalProperties* specifies, among others, the model used to compute the thermodynamic data. In this simulation, it is *janaf*. The specific heat capacity at constant pressure as well as the enthalpy (Eq. 2.37-Eq.2.38) are computed thanks to coefficients provided from NIST-JANAF tables and stored in *chemistry/thermoFile*.

$$\widetilde{c}_{p,s} = R \cdot \left[a_{0,s} + a_{1,s} \cdot \widetilde{T}_{1,s} + a_{2,s} \cdot \widetilde{T}^2_{2,s} + a_{3,s} \cdot \widetilde{T}^3_{3,s} + a_{4,s} \cdot \widetilde{T}^4_{4,s}\right] \tag{2.37}$$

$$\widetilde{h}_s = R\widetilde{T}_s \cdot \left[a_{0,s} + \frac{a_{1,s}}{2} \cdot \widetilde{T}_{1,s} + \frac{a_{2,s}}{3} \cdot \widetilde{T}^2_{2,s} + \frac{a_{3,s}}{4} \cdot \widetilde{T}^3_{3,s} + \frac{a_{4,s}}{5} \cdot \widetilde{T}^4_{4,s} + \frac{a_{5,s}}{\widetilde{T}_{5,s}}\right] \tag{2.38}$$

The mean mass fraction $\tilde{Y}_s$ ensues from its transport equation. With the mean reaction rate term $\overline{\rho}\widetilde{w}_s$ (defined in the next section) as the source term and the molecular diffusion coefficient $D_{m,s}$, the equation reads:

$$\frac{\partial \rho \widetilde{Y}_s}{\partial t} + \frac{\partial}{\partial x_j}(\overline{\rho}\widetilde{Y}_s \tilde{u}_j) = \frac{\partial}{\partial x_j}\left(\overline{\rho}\widetilde{D}_{m,s}\frac{\partial \widetilde{Y}_s}{\partial x_j} - \overline{\rho}\widetilde{Y_s"u_j"}\right) + \overline{\rho}\widetilde{w}_s \tag{2.39}$$

The modelisation of the effective diffusive flux to close the equation is similar to previous ones:

$$-\overline{\rho}\widetilde{Y_s"u_j"} = \frac{\mu_t}{Sc_t}\frac{\partial \widetilde{Y}_s}{\partial x_j} \tag{2.40}$$

With the turbulent Schmidt number $Sc_t = \frac{\nu_t}{\widetilde{k}}$ describing the ratio between the momentum and mass diffusivities.

2.1.4 Combustion model

The Eddy Dissipation Concept (EDC) models the turbulence-chemistry interactions in this simulation. It gives an expression of the mean reaction rate for RANS[21]. The EDC implies that each cell is decomposed into 2 regions (Fig. 2.1, based on De et al. [22]): a fine structure (reacting zone) and the surrounding fluid (non-reacting zone). The combustion is assumed to occur in these fine structures where the turbulent kinetic energy dissipates[22].

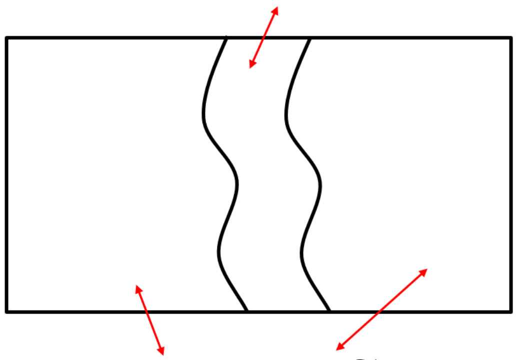

Figure 2.1: 2D Cell decomposition according to Eddy Dissipation Concept. With the mean reaction rate of specie s, $\widetilde{\dot{w}}_s$.

The model used in the simulation is its version of 2005 developed the same year by B. Magnussen[23]. However, unlike the original model, the Plug Flow Reactors (PFRs) approach describes the fine structures instead of the Perfectly Stirred Reactors (PSRs). In PFRs, the fluid mixing evolves axially but is assumed perfectly mixed radially. The evolution is expressed in terms of Ordinary Differential Equations (ODEs) with initial conditions, compared to non-linear algebraic equations system for PSRs which is solved by an iterative method[17]. Despite the higher computational cost of ODEs, they suit better with the In Situ Adaptative Tabulation method for chemistry (see section 2.1.5) which affects positively the computational efficiency.

Therefore, with PFRs consideration, the reactions evolve along the fine structures over the time scale. The following equations provide the mass fraction γ_λ and mean residence time τ^* of the fluid inside the fine structures:

$$\gamma_\lambda = C_\gamma \left(\frac{\nu \widetilde{\epsilon}}{\widetilde{k}^2} \right)^{\frac{1}{4}} \tag{2.41}$$

$$\tau^* = C_\tau \left(\frac{\nu}{\widetilde{\epsilon}}\right)^{\frac{1}{2}} \tag{2.42}$$

with the coefficients C_γ and C_τ, worth 2.1377 and 0.4083 respectively for the standard model. Modifications of these parameters is addressed in section 2.2.5. ν is the kinematic viscosity. $\widetilde{\mathrm{k}}$ and $\widetilde{\epsilon}$ are the solution of the k-ϵ model closure. Magnussen expressed the mean reaction rate of a specie s as:

$$\widetilde{\dot{w}}_s = -\frac{\overline{\rho}\gamma_\lambda^2}{\tau^*(1-\gamma_\lambda^2)} \cdot (\widetilde{Y}_s - Y_s^*) \tag{2.43}$$

Where $\widetilde{Y}_s$ results from the specie transport equation (Eq. 2.39). Thanks to the finite-rate chemistry, the fine structure mass fraction of the specie s, Y_s^*, ensues from the integration of:

$$\frac{\partial Y_s}{\partial t} = \frac{\dot{w}_s}{\rho} \tag{2.44}$$

$\dot{w}_s$, the instantaneous formation rate, is provided by the detailed chemical mechanism. The one used in this simulation is DRM19, containing 21 species and 58 reactions. Other more complex mechanisms exist (e.g. GRI3.0 - 53 species, 325 reactions), but DRM19 offers a reduced computational cost even if its temperature prediction accuracy is slightly lower than GRI3.0[12].

2.1.5 Tabulation of Dynamic Adaptive Chemistry

To reduce the computational cost of the simulation, the Tabulation of Dynamic Adaptive Chemistry (TDAC) assists the chemistry solver, namely *ode - Rosenbrock34*. The TDAC method includes tabulation and reduction mechanism approaches[24] (Fig. 2.2 [25]).

The first step uses In Situ Adaptive Tabulation (ISAT). It represents a storage of previous reactions with their initial composition and their result from the ODE integration. When a chemistry reaction with a composition ψ^q is ongoing, the ISAT module checks if it did not store the result of a previous similar reaction. If the difference in composition is under a certain threshold, the result is linearly approximated and reused $R^l(\psi^0)$. Otherwise, the costly ODE system is applied to find the solution. The new integrated result $\mathrm{R}(\psi_a^q)$ is stored to improve or enlarge the capacities of the ISAT module.
If it becomes necessary to determine the result of a reaction through the ODE system, the Dynamic Adaptive Chemistry (DAC) reduction module is applied. It focuses on local thermochemical conditions to produce a simplified reactions

mechanism. The species under a defined influence threshold are removed from the mechanism and the reaction concerns only the local species ψ_a^q. It reduces the cost of the ODE integration and as said previously, the result $R(\psi_a^q)$ is then stored in the ISAT module.

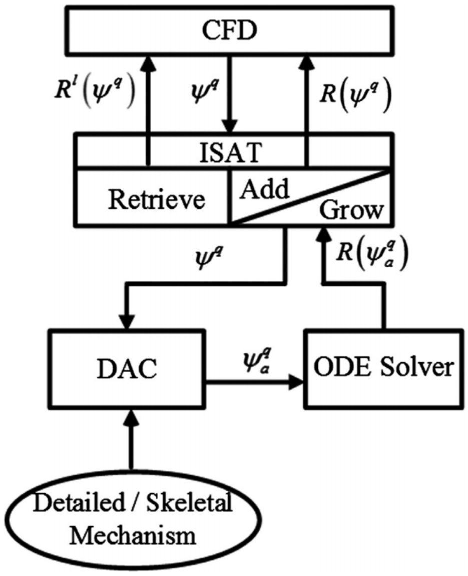

Figure 2.2: TDAC algorithm with ISAT and DAC modules.

The implementation of TDAC definitely alleviates the computational demand. The simulation converged twice faster for the DRM19 chemical mechanism[12]. The different settings such as the tolerances and the number of reactions stored can be adjusted in the *constant/chemistryProperties* file.

2.1.6 PIMPLE algorithm

The solving of the Navier-Stokes equations results from the Pressure Implicit Method for Pressure-Linked Equations (PIMPLE) algorithm. It is the combination of two other algorithms: PISO (Pressure Implicit with Splitting Operators) and SIMPLE (Semi-Implicit Method for Pressure-Linked Equations)[14]. After rewriting the momentum equation (Eq. 2.20) under matrix form (Eq. 2.45) with the FVM, a solution of the velocity field is found by using the pressure and density of the previous iteration in:

$$M \cdot \tilde{u} = R(p) \tag{2.45}$$

with M the coefficients matrix and R(p) the right-hand side of the momentum equation with the pressure component. This step is called the momentum prediction.

However, the computed velocity field $\tilde{u}^*$ could not fit the continuity equation (Eq. 2.19). There appears the pressure-velocity coupling that needs to be solved[26]. At first, it requires to rearrange the matrix M such that:

$$M \cdot \tilde{u}^* = D \cdot \tilde{u}^* - H(\tilde{u}^*) = R(p) \tag{2.46}$$

with D the diagonal matrix of M, H the residual matrix.
At this step, the residual matrix H is computed. Then, the previous expression is multiplied by the inverse matrix of D and with a second arrangement gives:

$$\tilde{u}^* = D^{-1}H(\tilde{u}^*) + D^{-1}R(p) \tag{2.47}$$

By substituting this expression in the continuity equation, it gives:

$$\frac{\partial \rho}{\partial t} + \frac{\partial}{\partial x_j}\Big(\rho(D^{-1}H(\tilde{u}^*) + D^{-1}R(p))\Big) = 0 \tag{2.48}$$

$$\frac{\partial \rho}{\partial t} + \frac{\partial}{\partial x_j}\left(\rho\frac{H(\tilde{u}^*)}{d_p}\right) = -\frac{\partial}{\partial x_j}\left(\rho\frac{R(p)}{d_p}\right) \tag{2.49}$$

with $\frac{1}{d_p} = D^{-1}$. A new guess on the pressure is made with this last equation and a correction on the velocity field can be operated:

$$\tilde{u}^{**} = D^{-1}H(\tilde{u}^*) + D^{-1}R(p^*) \tag{2.50}$$

This new velocity field would allow a better approximation of the pressure. Therefore, inner and outer loops are added. They are characteristic to the PISO and SIMPLE algorithms respectively, and the PIMPLE is composed of both. The inner loop reuses $\tilde{u}^{**}$ and the corrected pressure to compute the residual matrix with Eq. 2.46 and to perform the next steps. While the outer loop reuses $\tilde{u}^{**}$, the corrected pressure and density back to the momentum prediction. To compute the density, the energy and specie equations are solved after the velocity correction. With the resulting temperature and species mass fraction, the density is derived thanks to the perfect gas relation (specified in *constant/thermophysicalProperties* file). The steps are summarised in Fig. 2.3[27][14].

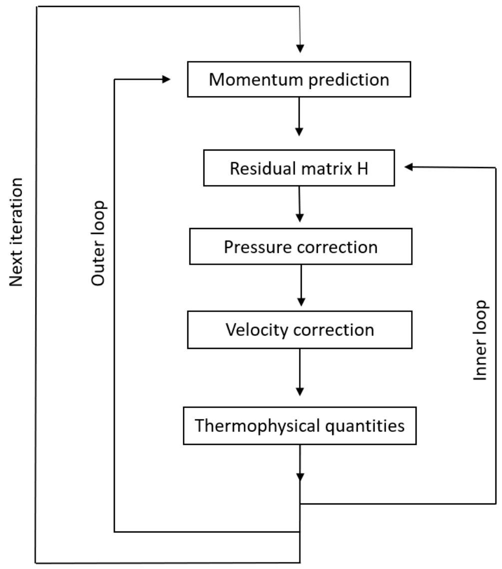

Figure 2.3: PIMPLE algorithm.

The PIMPLE settings are specified in *system/fvSolution* file. The ones of the simulation developed by Dr. Z. Li are in Table 2.3.

nCorrectors	nOuterCorrectors
2	1

Table 2.3: Number of inner (nCorrectors) and outer (nOuterCorrectors) loops in the PIMPLE algorithm for non-uniform boundary conditions simulation.

With nCorrectors > 1 and nOuterCorrectors $= 1$, it makes the PIMPLE algorithm equivalent to the PISO one.

2.1.7 Geometry

A DJHC burner geometry was chosen to model the regime (Figure 2.4)[2]. The burner is simplified for the simulation and is represented as a cylinder with three inlets: a central fuel inlet, surrounded by the coflow and then the air. The outer radius is 80 [mm] and the length 225 [mm].

[2]The secondary burners use the same fuel as the primary fuel inlet, namely the Dutch natural gas (mixture of ethane, methane and nitrogen).

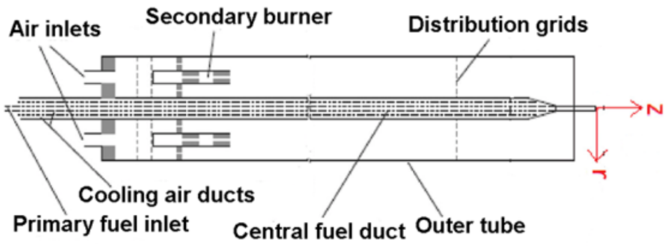

Figure 2.4: Schematic of a Delft Jet in Hot Coflow burner

The axi-symmetry of the geometry allows to decrease the computational cost of the simulation by considering only a wedge of the cylinder (Fig. 2.5). Its angle is computed in section 2.2.1. This wedge is then decomposed into cells of small size for the FVM. While the longitudinal step between the cells is constant, the radial step is different for the three inlets (Table 2.4). Note that a wedge is one cell thick[28].

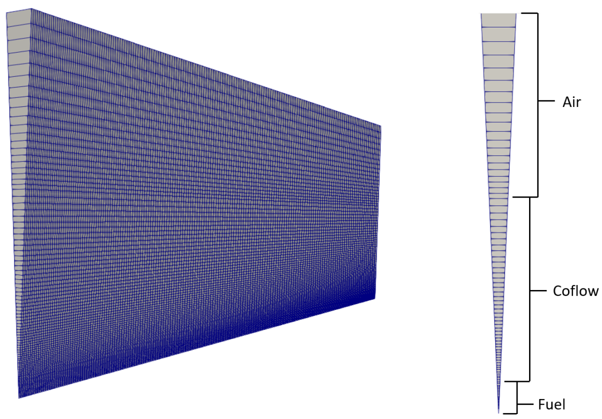

Figure 2.5: Case geometry - wedge with cells (left). Wedge inlet patches decomposition (right).

Two regions need to be identified. At first, the planar faces at the boundaries of the mesh are referred as the boundaryField. It is composed of *patches* that are a series of linked faces (Fig. 2.6). This is where the boundary conditions are set. Then there is the internalField, composed of every cells of the mesh. With 90 radial and 160 longitudinal cells, 14 400 compose this region.

Patch	r_1 [mm]	r_{end} [mm]	cells
Fuel	0	2.5	10
Coflow	2.5	43	60
Air	43	80	20
Outlet	0	80	90
	x_1 [mm]	x_{end} [mm]	
Top	0	225	160

Table 2.4: Wedge dimensions.

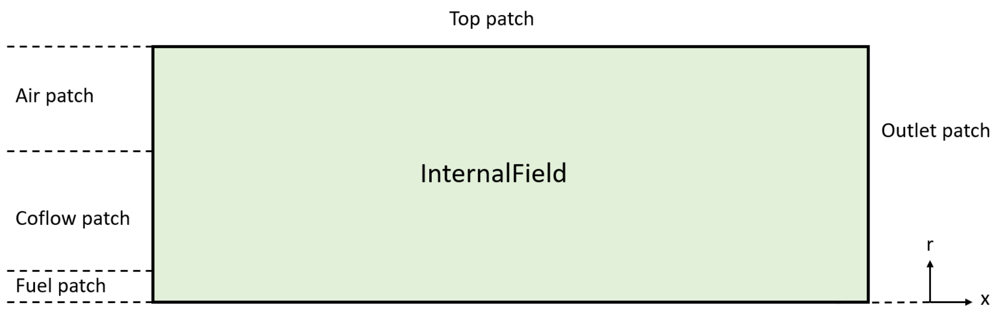

Figure 2.6: Longitudinal cut of the wedge. BoundaryField (made of patches) and internalField.

2.2 Modifications

2.2.1 Uniform boundary conditions

The boundary conditions of the system can be adjusted in the folder *0*. In this latter, there is a file for each parameter involved in the simulation where their values and distributions for the internalField and the boundaryField patches can be specified. Every patch can have its own distribution type. In case of non-uniform type, a value is assigned for each cell. By setting the type to uniform, it requires one entry to specify the value of every cells of the patch. It definitely eases the work for the upcoming UQ analysis which required parameters value changes, besides the justified guess for the burner inlet distribution.

To obtain a first idea on the parameters value in uniform conditions, a weighted average is performed on the non-uniform values. The arithmetic mean could not be retained as the cells have different volumes and planar surfaces at the patches.

For the boundaryField, only cells surface at the boundaries are considered and the weighted average for a quantity ϕ is given by:

$$\phi_{uniform} = \sum_{i=1}^{N} \frac{\phi_i \cdot A_{i,patch}}{A_{tot,patch}} \tag{2.51}$$

with N the number of patch cells.
The surface computation requires the wedge angle θ. The data provided on the geometry in the *constant/polyMesh/blockMeshDict* file allows to find it:

Trigonometry gives the half-angle α:

$$\alpha = atan\left(\frac{3.489}{79.9238}\right) = 2.4996°$$

The wedge total angle is then:

$$\theta = 2\alpha = 5°$$

The surfaces can now be found using the wedge-cylinder ratio of $\frac{5}{360}$.

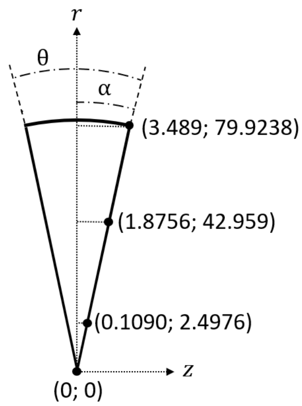

Figure 2.7: Schematic of wedge radial cut.

Inlet and outlet patches

For the fuel, coflow and air, it gives:

$$A_i = \pi \cdot (r_{i+1}^2 - r_i^2) \cdot \frac{5}{360}$$

$$A_{tot} = \pi \cdot (r_{end}^2 - r_1^2) \cdot \frac{5}{360}$$

The outlet cells distribution is the combination of the three inlet patches.

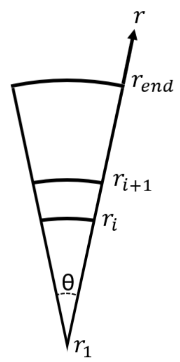

Figure 2.8: Schematic of inlet and outlet patches.

Top patch

The surface of the top patch corresponds to the external surface of the wedge:

$$A_i = 2\pi \cdot r_{end} \cdot (x_{j+1} - x_j) \cdot \frac{5}{360}$$

$$A_{tot} = 2\pi \cdot r_{end} \cdot (x_{end} - x_1) \cdot \frac{5}{360}$$

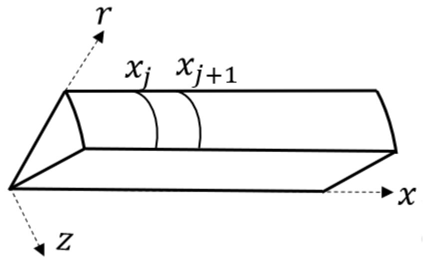

Figure 2.9: Schematic of top patch.

The lateral patches of the wedge, namely *front* and *back*, do not require any value but they need to be referred as *wedge* type.
For the internalField, the cells volume is considered and weighted average of a quantity ϕ is then:

$$\phi_{uniform} = \sum_{i=1}^{N} \sum_{j=1}^{K} \frac{\phi_{i,j} \cdot V_{i,j}}{V_{tot}} \tag{2.52}$$

InternalField

Volume of each cell in the field:
$V_{i,j} = [(\pi \cdot r_{i+1}^2 \cdot (x_{j+1} - x_j) - (\pi \cdot r_i^2 \cdot (x_{j+1} - x_j)] \cdot \frac{5}{360}$

$V_{tot} = \pi \cdot r_{end}^2 \cdot (x_{end} - x_1) \cdot \frac{5}{360}$

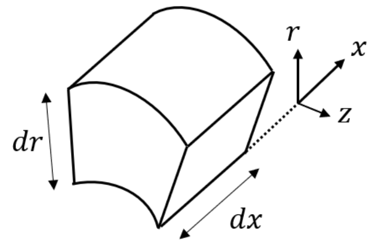

Figure 2.10: Schematic of a cell.

The function *BC_integrals.py* computes the weighted average of any parameter with a non-uniform distribution at the internalField and/or boundary patch. The results are written in text file *resultIntegrals.txt* (Appendix B). A new folder containing the uniform boundary conditions is then created, namely *0.uniform.* The latter serves then as a basis to develop the boundary and the initial conditions of the simulation to make it converge faster.
Note that to ease the work, the function *removeInternalField.py* allows to remove the 14 400 cells values of the internalField found in almost every file of the non-uniform case.

2.2.2 Clean burner start

What is meant behind the clean burner idea is that no intermediate species and the least physical properties inside the burner should interfere in the flow development. It allows to make the simulation converge quicker towards its own flow field by starting from a configuration closer to its final one.

The values in the internalField are initial conditions to launch the simulation. In the present case, they are assumed at ambient conditions and the burner only filled with air (Table 2.5). All other specie mass fraction are set to 0. Quantities such as the mean velocity, the mean turbulent kinetic energy k and its dissipation rate ϵ of the internalField keep their uniform value to start the simulation. It slows the convergence but it appeared convenient to run the simulation as no information could be obtained on the flow field with only an air jet.
The boundary conditions at the top patch were not changed and they keep their uniform value. Table 2.6 gathers the inlets boundary conditions with non-zero values. Also, different inputs were removed from the set provided in the folder *0* as they can be computed from other quantities already present or they are not anymore relevant when starting from a clean burner:

- Density ρ: computed with the perfect gas relation thanks to the pressure, temperature and species mass fraction.
- Massflow ϕ: computed from the known geometry, velocity and the previously calculated density, $\phi_i = \rho_i \cdot U_i \cdot A_i$
- Heat released dQ and its rate $\dot{Q}$: Initially, no heat is produced nor released, they can be either set to 0 or removed.

Thanks to *turbulentIntensityKineticEnergyInlet* and *turbulentMixingLengthDissipationRateInlet*, the values of k and ϵ (for the coflow and air) are expressed in terms of their intensity I and mixing length L, respectively, according to:

$$k = \frac{3}{2} \cdot (I \cdot |U|)^2 \tag{2.53}$$

$$\epsilon = \frac{C_\mu^{0.75} \cdot k^{1.5}}{L} \tag{2.54}$$

with the model coefficient $C_\mu = 0.09$. I and L are computed (Table 2.7) from the uniform values of k and ϵ present in Appendix B.

Parameter	Value	SI & Description
Y_{O_2}	0.21	Mass fraction [-]
Y_{N_2}	0.79	Mass fraction [-]
p	100 000	Operating pressure [Pa]
T	293	Temperature [K]
k	0.3115	Turbulent kinetic energy [m^2/s^2]
ϵ	117.46	Dissipation rate of k [m^2/s^3]
U	(1.64, -0.053, -1.38e-13)	Velocity [m/s]

Table 2.5: Initial conditions (ambiant) in the internalField (mean values).

Parameter	Fuel	Coflow	Air	SI & Description
Specie				
$Y_{C_2H_6}$	0.066			Mass fraction [-]
Y_{CH_4}	0.706			Mass fraction [-]
Y_{CO}		1e-05		Mass fraction [-]
Y_{CO_2}		0.095		Mass fraction [-]
Y_{H_2O}		0.081		Mass fraction [-]
Y_{N_2}	0.228	0.746	0.79	Mass fraction [-]
Y_O		1e-05		Mass fraction [-]
Y_{O_2}		0.076	0.21	Mass fraction [-]
Y_{OH}		0.00028		Mass fraction [-]
Thermodynamic quantities				
p	100 000	100 000	100 000	Operating pressure [Pa].
T	566	1358	293	Temperature [K]
α_t	1.0786e-04	1.0673e-04	1.1178e-04	Turbulent thermal diffusivity [m^2/s]
ν_t	1.0786e-04	1.0673e-04	1.1178e-04	Turbulent kinematic viscosity [m^2/s]
Flow quantities				
U	(22.575, 0, 0)	(3.502, 0, 0)	(0.5, 0, 0)	Velocity [m/s]
k	7.1954	Table 2.7	Table 2.7	Turbulent kinetic energy [m^2/s^2]
ϵ	32561.39	Table 2.7	Table 2.7	Dissipation rate of k [m^2/s^3]

Table 2.6: Inlet boundary conditions of non-zero parameters (mean values).

	Coflow	Air
L [mm]	0.007306	0.004956
I [%]	0.019209	0.06

Table 2.7: Mixing length and turbulent kinetic energy intensity for Coflow and Air patches.

The jet Reynolds numbers, deduced from Table 2.6 and the hydraulic diameters D_h, show that the simulation performs under quite low Reynolds (Table 2.8). The turbulence is enhanced by the shear stress between the different flows.

$$Re = \frac{U \cdot D_h}{\nu_t} \tag{2.55}$$

	Fuel	Coflow	Air
D_h [mm]	5e-03	38e-03	37e-03
Re [-]	1046	1246	165

Table 2.8: Reynolds number of different inlet jets

with D_h = D for a circular pipe (fuel) and $D_h = D_{out} - D_{in}$ for an annular pipe (coflow and air).

2.2.3 Convergence

When starting from new boundary conditions (clean burner), it becomes necessary to assess the convergence of the simulation as the study of a steady field is wanted. However, the computational cost of the simulation is expensive. A trick consists to develop the flow field without chemistry at first, to evaluate its convergence and then to switch on the chemistry. This way, the significant computational demand induced by the chemistry is reduced by starting from a field closer to the final solution.

- <u>Convergence without chemistry</u>

  The technique used for the part without chemistry is the residuals. They are a measure of imbalance in the solution of the model equations as iterations progress. The imbalance here defines the difference between two consecutive initial iterations (the current and previous ones). While the accuracy of the simulation is assessed through small value of the residuals (in general, order of at least 1e-3), the convergence can be evaluated through a stable trend in the plot.

  In the present case, the residuals were evaluated for 40 000 intervals. A stable trend appeared from the 36 000th but the values oscillate around 1e-2. Still, it is considered admissible to carry on the present work and the chemistry is switched on from the 40 000th interval. In a try to improve the prediction of the algorithm, the number of inner loops was increased by one increment in the PIMPLE algorithm. The predictions for the third iteration were slightly better but the same trend remained.

- <u>Convergence with chemistry</u>

  To evaluate the convergence with chemistry, the temperature profiles through time give a good indication on the combustion progress. The following graphs are radials cuts taken at different axial position in the burner (see section 2.2.4).

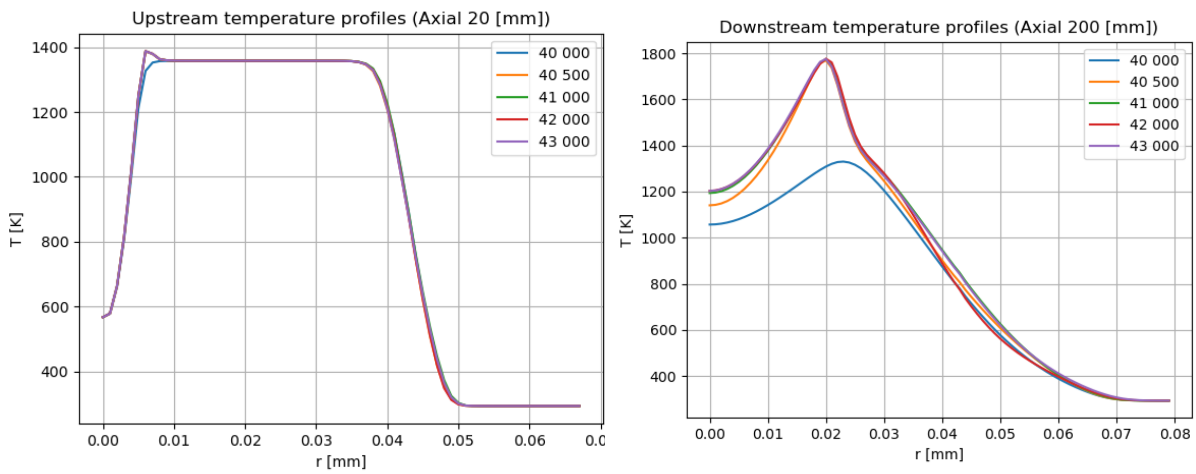

Figure 2.11: Upstream and downstream radial cuts of the mean temperature evolution through time. Uniform boundary conditions simulation with chemistry.

The flow with chemistry was developed for 3000 intervals more. The upstream flow converges quickly while the downstream flow with more complex reactions requires more time. The central region converges after 1000 intervals but the other side of the flame present an oscillation at the 42 000th interval. This instability was also seen on the corresponding residuals graph. However the latter confirmed the convergence at the 43 000th interval.

The Table 2.9 resumes the control settings of the 2 simulations. The discretisation schemes and turbulence model coefficients are respectively in Table 2.1 page 7 and Table 2.2 page 11. Before switching to the statistical analysis, a comparison is made between the steady state fields of the two simulations to assess the validity of the new boundary conditions.

	Uniform		Non-uniform	
Time				
	Start	End	Start	End
No chemistry	0	40 000	/	/
Chemistry	40 000	43 000	0	3000
PIMPLE				
nCorrectors	3		2	
nOuterCorrectors	1		1	
EDC				
C_γ	2.1377		2.1377	
C_τ	0.4083		0.4083	
Detailed chemical mechanism	DRM19		DRM19	
TDAC	Active		Active	

Table 2.9: Uniform and Non-uniform boundary conditions simulation initial settings (time, algorithm and combustion model).

2.2.4 First results

The comparison between the two simulations allows to evaluate the validity of the uniform boundary conditions simulation which is further used for the statistical analysis. Differences are expected as the inlets distribution underwent significant changes. The results are shown as radial cuts taken at different axial locations with the centerline corresponding to the x-axis (Fig. 2.12). The studied fields are the 3000^{th} and $43\ 000^{th}$ time interval of the non-uniform and uniform boundary conditions simulation respectively.

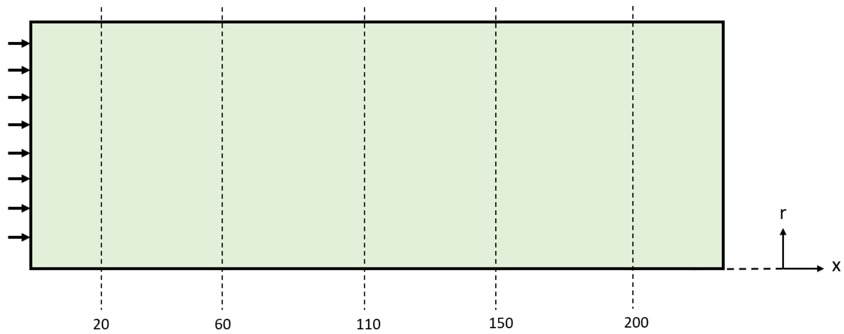

Figure 2.12: Different axial locations (in [mm]) of the radial cuts.

The flow field is evaluated through temperature and velocity profiles, which give a look on both heat transfer and fluid dynamics. Attention is also brought on the OH mass fraction field which, by being a main radical in methane combustion, gives an insight on the flame structure.

Upstream, the mean temperature cuts (Fig. 2.13) show the characteristics of the uniform boundary conditions. The emerging peak temperature is significantly lower than the one for non-uniform boundary conditions but the gap shrinks as the flow goes downstream. At an axial location of 200 [mm], the temperature profile is not fully developed yet, unlike for the non-uniform inlets. In both cases, the air buffer maintains a relatively low temperature at the wall (which allows to prevent stresses) and the central region heats up of hundreds of Kelvin. Still, a lower temperature rise is noticed for uniform inlets despite a higher starting value.

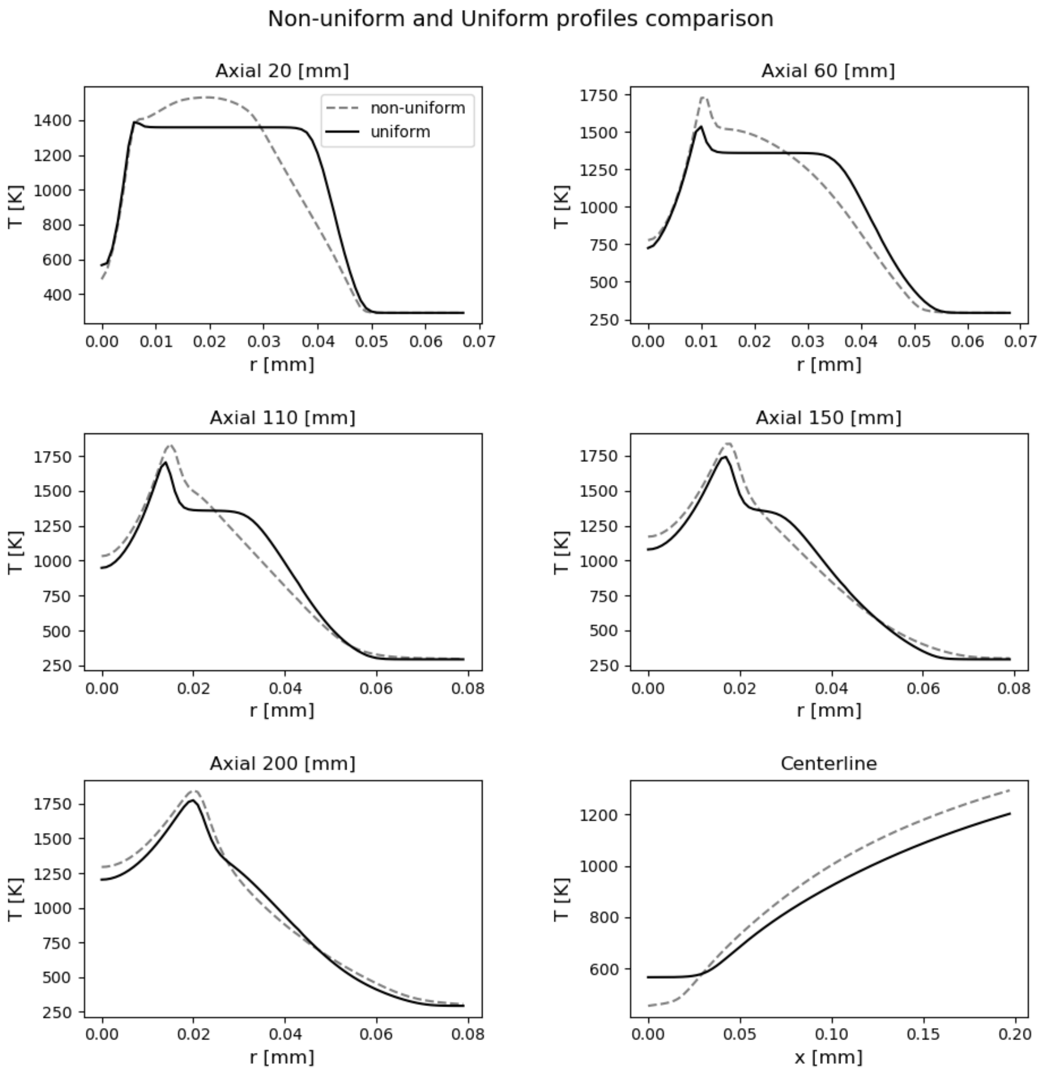

Figure 2.13: Mean temperature T [K] profiles for radial cuts at different axial location and for the centerline. Comparison between uniform and non-uniform boundary conditions. Standard EDC coefficients.

The uniform case implies significant changes upstream. The flow takes more time to dissipate the characteristics of the inlets but while differences remain, the flows tend towards the same mean temperature profiles downstream.

In terms of mean axial velocity U_x [m/s] profiles (Fig. 2.14), the same conclusions as for the temperature can be drawn. While different profiles appear due to the different distributions, the velocity field takes longer to develop for the uniform inlets and still presents characteristics of those downstream. However, the gap in the central region decreases drastically and both boundary conditions reach the same order of magnitude downstream.

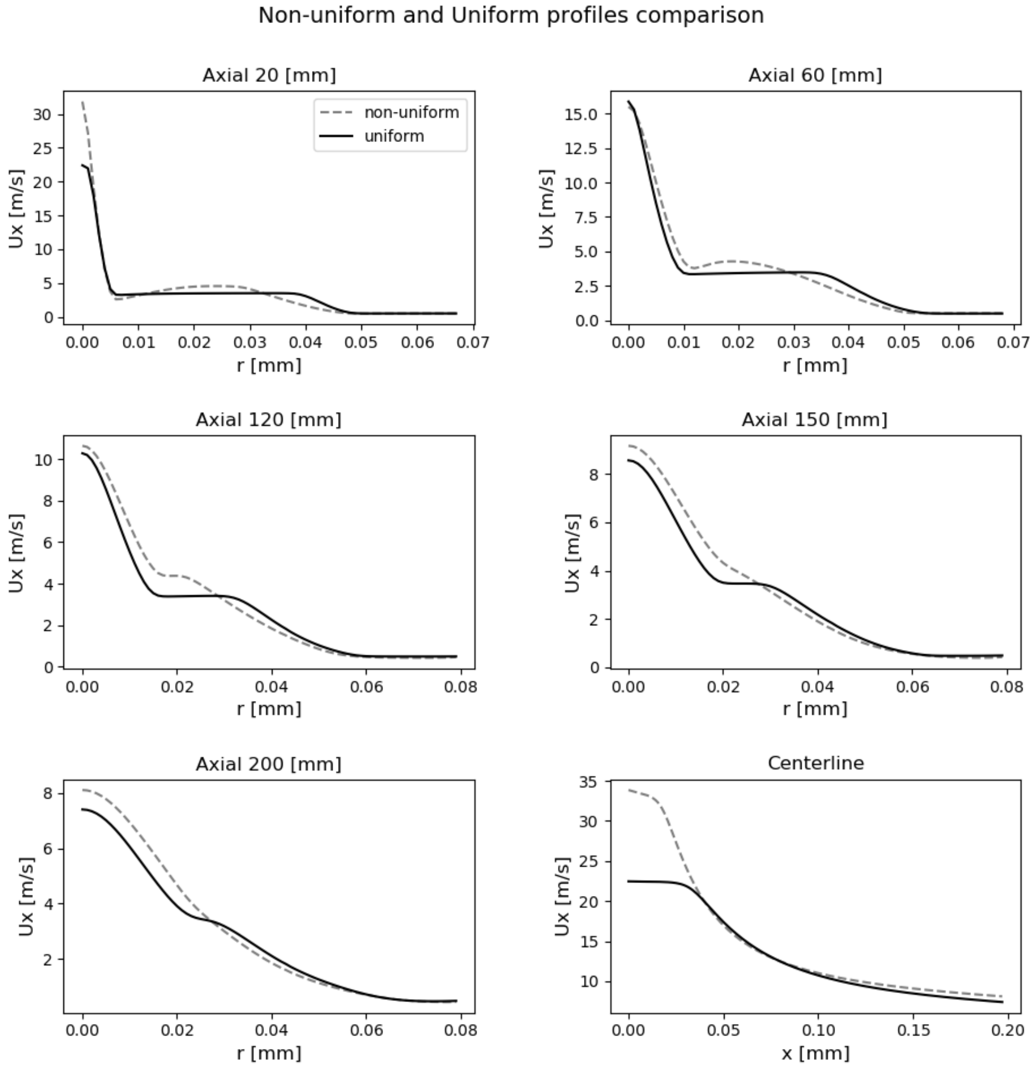

Figure 2.14: Mean axial velocity U_x [m/s] profiles for radial cuts at different axial location and for the centerline. Comparison between uniform and non-uniform boundary conditions. Standard EDC coefficients.

The OH mass fraction Y_{OH} [-] cuts (Fig. 2.15) underline again that despite a distinguishable difference in the distribution upstream, both simulations reach similar profiles downstream. Then, the Y_{OH} peak indicates that the flame evolves progressively and radially for uniform and non-uniform boundary conditions. The mass fraction in the central region is negligible. It leads to the conclusion that reactions occur in a thin layer going away of the primary energy source, as it can be seen on the temperature and heat released fields (Fig. 2.16-2.17).

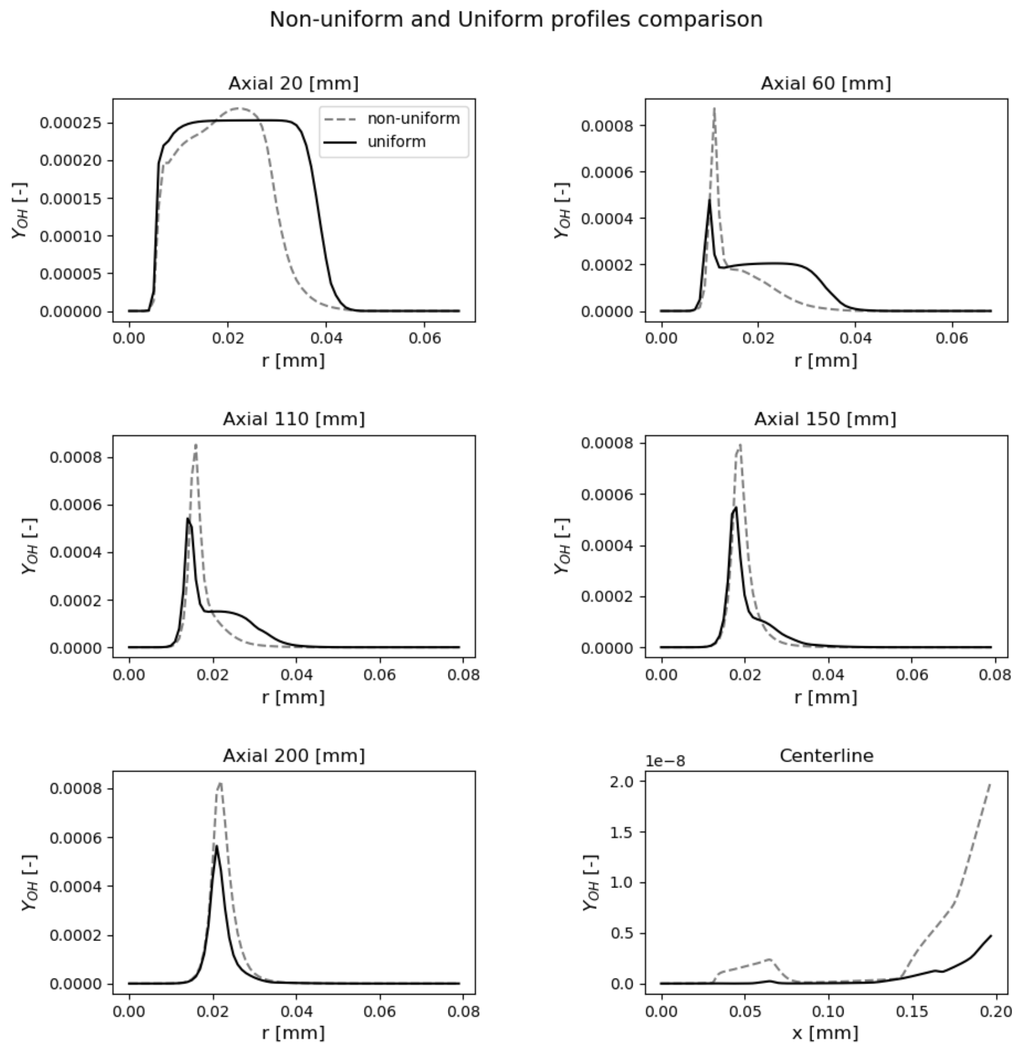

Figure 2.15: Mean OH mass fraction Y_{OH} [-] profiles for radial cuts at different axial location and for the centerline. Comparison between uniform and non-uniform boundary conditions. Standard EDC coefficients.

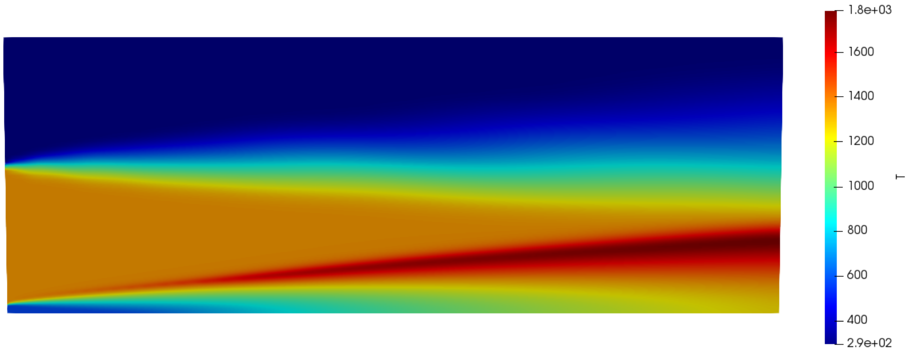

Figure 2.16: Mean temperature T [K] field in the wedge. Uniform boundary conditions, standard EDC coefficients.

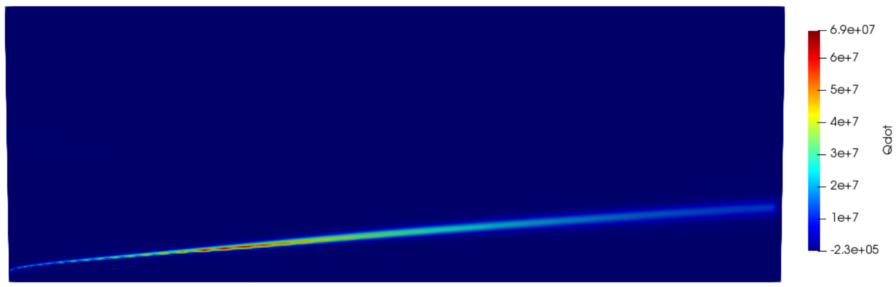

Figure 2.17: Mean heat released rate $\dot{Q}$ [W/m^3] in the wedge. Uniform boundary conditions, standard EDC coefficients.

The analysis of the previous quantities at different locations of the burner demonstrated a similar combustion behaviour (heat transfer, temperature peak, fluid dynamics and flame structure) for the uniform inlets compared to the non-uniform ones. To apply uniform boundary conditions on the simulation seems therefore a reasonable trade-off between accuracy of the simulation and possibility to ease the work for the UQ analysis.

However, the temperature peak in the reaction zone which is seen on the downstream temperature cuts or on the heat released field with a kernel of higher density, results from an over-prediction of temperature by the combustion model. The next section addresses this issue.

2.2.5 Combustion model adjustment

MILD combustion is characterised by a distributed reaction zone, but the first results showed a significant temperature peak in the flame region. Aminian et al. [29] state that the source of this issue comes from an over-prediction of the temperature by the EDC model which was developed under different conditions than the one of MILD combustion. An adjustment of the model coefficients (C_γ, C_τ) helps to improve the temperature prediction. In her work[12], Dr. Z. Li tested the following settings based on the work of De et al.[22]:

Coefficients	Standard	Adjustment 1	Adjustment 2	Adjustment 3
C_γ	2.1377	1.0	1.0	1.0
C_τ	0.4083	0.4083	1.47	3.0

Table 2.10: EDC coefficients settings.

First, by reducing C_γ, the mass fraction inside the fines structures is lower (Eq. 2.41). It induces less reactions, therefore less heat released and the temperature decreases. C_γ is then fixed and it is the residence time in the fines structures which is raised through the increase of C_τ (Eq.2.42). The mean reaction rate (Eq.2.43) decreases and so does the temperature. An extinguished flame appeared for the third adjustment but the second one replicated better the experimental data[12]. Therefore, second adjustment was performed on the uniform boundary conditions simulation (Fig. 2.19). As expected, the temperature peak decreases, accompanied of a slight radial shift. Consequently, the temperature field is more homogeneous in the reaction zone (Fig. 2.18) and the flame region with higher energy density is wider (Fig. 2.20). A decrease is also noticed for the value of the central region.

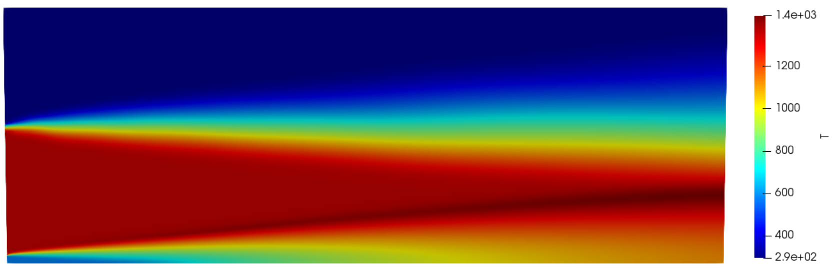

Figure 2.18: Mean temperature T [K] field. Uniform boundary conditions, 2^{nd} adjustment of EDC coefficients.

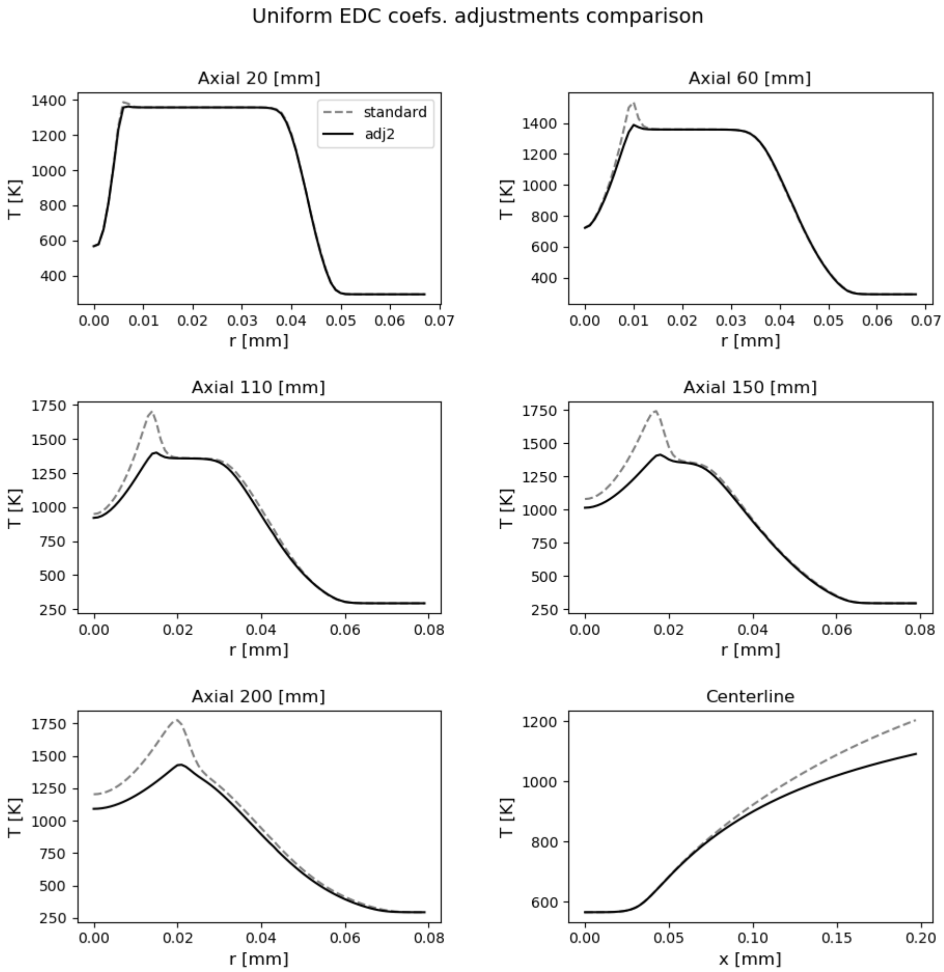

Figure 2.19: Mean temperature T [K] profiles with EDC coefficients adjustments. Uniform boundary conditions.

The high temperatures reached with the standard coefficients favour the production of CO, a result of incomplete combustion. Indeed, CO_2 becomes unstable and dissociates into:

$$CO + \frac{1}{2}O_2 \Leftrightarrow CO_2$$

$$CO_2 + H_2 \Leftrightarrow CO + H_2O$$

With a decrease of $\approx 350[K]$ in the temperature peak induced by the 2^{nd} adjustment, the CO production is also drastically reduced (Fig. 2.21 - 2.22). Note that CO also comes from the coflow as seen in Table 2.6 but in rather poor quantity.

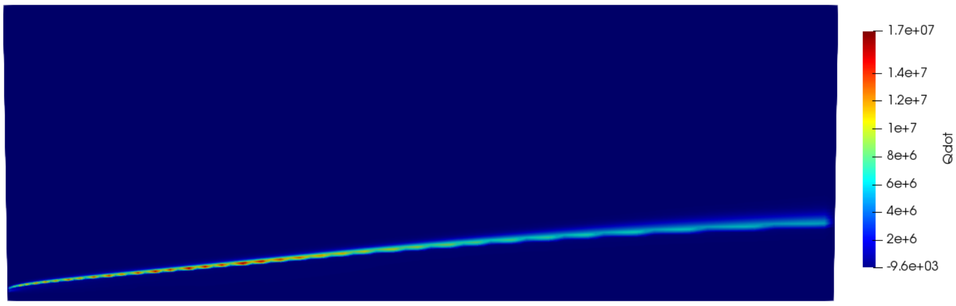

Figure 2.20: Mean heat released rate $\dot{Q}$ [W/m^3] field. Uniform boundary conditions, 2^{nd} adjustment of EDC coefficients.

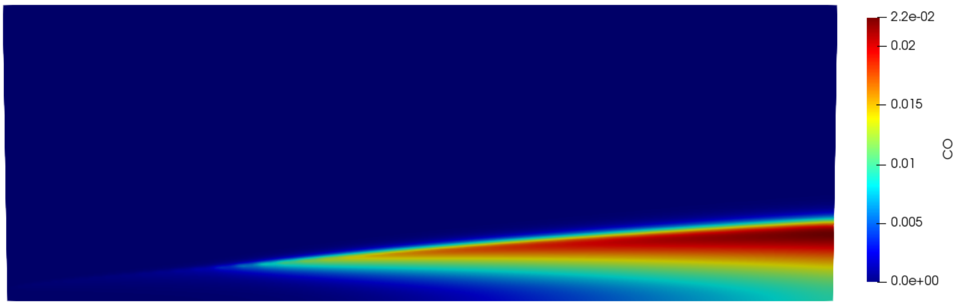

Figure 2.21: Mean CO mass fraction Y_{CO} [-] field. Uniform boundary conditions, standard EDC coefficients.

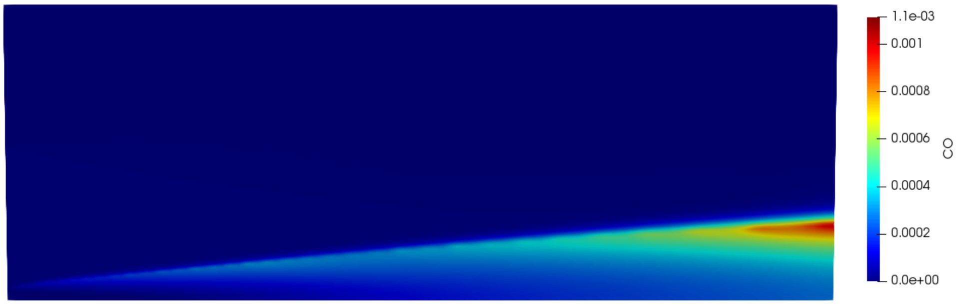

Figure 2.22: Mean CO mass fraction Y_{CO} [-] field. Uniform boundary conditions, 2^{nd} adjustment of EDC coefficients.

2.2.6 Summary

A change in the boundary conditions of the reference simulation had to be done to carry out the UQ analysis. By setting them to uniform, OpenFOAM requires one entry value per patch, which is then assigned to each of its cells. A weighted average was then performed on the non-uniform boundary conditions to obtain the single uniform value. With this new distribution at the inlets, the flow field is expected to present its own characteristics. Therefore, to make the simulation converge faster, the latter starts from a clean burner without chemistry first. Arrived at the 40 000^{th} interval, the chemistry is activated and the downstream flow needs 3000 intervals more to converge.

The first results of the uniform boundary conditions have shown a satisfactory behaviour in terms of heat transfer, fluid dynamics and flame structure. With a modification of the combustion model constants to alleviate its temperature over-prediction, the simulation is set up for the upcoming statistical analysis.

Chapter 3

Uncertainty quantification

A mathematical representation, or a model, of a physical phenomena builds outputs from a set of inputs. The objective of a global sensitivity analysis is to quantify the relative importance of each input on the output(s) of interest and to build a surrogate model. In the present work, it is achieved through a non-intrusive Polynomial Chaos Expansion. The chapter first gives a mathematical background on the PCE, before to address the selection the outputs and inputs of interest for the study. Follows the definition of the uncertainties intervals, which shows the limitation of the current simulation.

3.1 Polynomial Chaos Expansions

To propagate the uncertainties, the RHEIA framework uses the polynomial chaos expansion method described hereafter. Given the software used for the CFD simulation, it is not possible to connect this latter to the framework. The different steps required for such case are listed at the end of the section.

3.1.1 Mathematical model

The PCE models the outputs of interest in a series of multivariate orthogonal polynomials ψ and corresponding deterministic coefficients a:

$$M(\xi) = \sum_{i=0}^{\infty} a_i \ \psi_i(\xi) \tag{3.1}$$

with ξ the independent Sobol sequenced input variables.

Sobol sequence is a quasi-random sampling method allowing a faster convergence due to a lower discrepancy ("clustering effect") than with random sampling (Fig. 3.1 [30]). Details on the method can be found in [11].

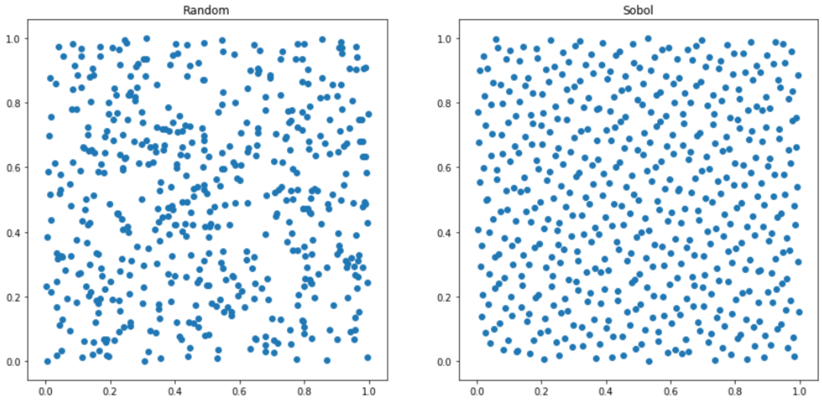

Figure 3.1: Random (left) vs Sobol (right) sampling method.

The polynomials in Eq. 3.1 belong to the Wiener-Askey family for which the orthogonality reads[31]:

$$< \psi_i \psi_j >=< \psi_i^2 > \delta_{ij} \tag{3.2}$$

with the Kronecker delta function δ_{ij}.
The probability distribution of the polynomials is also known with regards to the distribution of ξ. In the present work, their distribution is uniform.
Nonetheless, the previous modelisation is obtained with an infinite series. To reduce the computational demand, a truncation scheme is applied on the polynomial order p of the expansion such that:

$$\sum_{\alpha=0|\alpha\in A}^{P} a_\alpha \ \psi_\alpha(\xi) = M^{pce}(\xi) \approx M(\xi) \tag{3.3}$$

with α the multi-indices in the set A for which the size is defined as:

$$card(A^{d,p}) = P + 1 = \frac{(d+p)!}{d! \ p!} \tag{3.4}$$

where d is the number of uncertain parameters.
To evaluate the coefficients, the RHEIA framework employs a non-intrusive regression method so that no modification needs to be applied on the computational model.

The method is the Least-Square Minimisation (LSM). To be well-posed, it requires a number of evaluations (n) at least twice as big as the set of multi-indices:

$$n = 2 \cdot card(A^{d,p}) = 2 \cdot \frac{(d+p)!}{d!\ p!} \tag{3.5}$$

The LSM aims at reducing the mean square error E[ϵ^2] resulting from the truncation, which is defined as:

$$E[\epsilon^2] = E\left[(M(\xi) - M^{pce}(\xi))^2\right] = E\left[\left(M(\xi) - \sum_{\alpha=0|\alpha\in A}^{P} a_\alpha\ \psi_\alpha(\xi)\right)^2\right] \tag{3.6}$$

In other words, it aims at finding the set of coefficients a such that:

$$a = argmin\ \frac{1}{n}\sum_{i=1}^{n}\left(M(\xi^{(i)}) - \sum_{\alpha\in A} a_\alpha\ \psi_\alpha(\xi^{(i)})\right)^2 \tag{3.7}$$

It is achieved by rewriting Eq. 3.3 under matrix form:

$$G \cdot a = b \tag{3.8}$$

with:

- G = $\{G_{ij} = \psi_j(\xi^{(i)})$; i=1...n, j=1...card($A^{d,p}$)}
- b = $\{b^{(1)} = M(\xi^{(1)})$,...$b^{(n)} = M(\xi^{(n)})\}$

Then, the solution of the LSM ensues from:

$$a = (G^T G)^{-1} G^T b \tag{3.9}$$

With the coefficients hence computed, the statistical moments (mean μ, variance σ^2) are derived:

$$\mu = a_0 \tag{3.10}$$

$$\sigma^2 = \sum_{i=1}^{P} a_i^2 \tag{3.11}$$

The total impact of an uncertainty on the stochastic output is then obtained with the Sobol indices. It corresponds to the ratio between the variance of the uncertainty and the variance of all uncertainties :

$$Sobol_u^{t,pce} = \frac{\sigma^2(\xi_u)}{\sum_{u=1}^{d} \sigma^2(\xi_u)} = \frac{\sum_{i=1}^{P} a_{u,i}^2}{\sum_{u=1}^{d} \left(\sum_{i=1}^{P} a_{u,i}^2 \right)} \tag{3.12}$$

The accuracy of the surrogate model ensues from the Leave-One-Out (LOO) cross validation error. In definition, the LOO error reads:

$$\hat{\mathrm{E}}_{LOO} = \frac{1}{n} \sum_{j=1}^{n} \Delta_j^2 \tag{3.13}$$

with Δ_i the residual error. Using the full experimental design of ξ, it reads:

$$\Delta_i = \frac{M(\xi^{(i)}) - M^{pce}(\xi^{(i)})}{1 - h_i} \tag{3.14}$$

with h_i the diagonal terms of $G(G^T G)^{-1} G^T$.
The LOO error is then normalised by the variance to finally give:

$$\hat{\epsilon}_{LOO} = \frac{\frac{1}{n} \left(\sum_{i=1}^{n} \frac{M(\xi^{(i)}) - M^{pce}(\xi^{(i)})}{1 - h_i} \right)}{Var(b)} \tag{3.15}$$

Typically, an error of 1% is admissible. Higher, it requires to increase the polynomial order which implies more evaluation to make (Eq. 3.5). Hopefully, the PCE allows to reuse the training set of the previous polynomial order.

3.1.2 Steps to follow in the present work

RHEIA achieves a major part of the previous computation. The remaining steps that one must conduct for an unconnected model are the following:

1. To define independent uncertain parameters and output(s) of interest (sections 3.2-3.3).
2. To define the stochastic spaces of the uncertainties (section 3.4).
3. To generate the samples with RHEIA (section 3.4).
4. To run the simulations under the different samples.

5. To collect the output(s) of interest and to connect them to the corresponding samples.

6. The Sobol, statistical moments and error are then computed with RHEIA. Note that with the computational demanding simulation used in this work, a greater tolerance for the error could be accepted (depending on the results).

3.2 Markers: Outputs of interest

The present study aims at covering the combustion process under different aspects. To do so, four markers are used: the combustion efficiency, the fuel consumption, the maximal temperature and the flame width. This section describes them all as well as the extraction procedure of the corresponding necessary values.

1. **Combustion efficiency**
   MILD combustion is qualitatively expected to produce high efficiency while emitting low amount of pollutants[3]. However, only the thermal efficiency is provided in the literature and no value could be found for the combustion efficiency. Therefore, the focus is put on the variations of the combustion heat released rate to quantify η_{comb} and to obtain insights on its main drivers:

$$\eta_{comb} = \frac{Heat\ released\ rate}{Primary\ power} = \frac{\dot{Q}}{\dot{m}_{fuel} \cdot LHV} \tag{3.16}$$

   with $\dot{m}_{fuel}$ the total fuel massflow and LHV its Lower Heating Value, the energy that would be released by a fuel unity for a complete combustion.

   The initial primary power of the burner is known. Before to compute it, a distinction needs to be made between $\dot{m}_{fuel}$ and ϕ_{fuel}. ϕ_{fuel} is the uniform value assigned for each cell of the corresponding patch and was computed in section 2.2.1 but it does not represent the total amount of fuel entering in the wedge. The mass flow is an extensive variable and the contribution of each cell (10) needs to be taken into account:

$$\dot{m}_{fuel,wedge} = 10 \cdot \phi_{fuel} = 10 \cdot 2.853 \cdot 10^{-7} = 2.853 \cdot 10^{-6}\ [kg/s]$$

   The fuel LHV ensues from its composition (Table 2.6): 70.6% CH_4, 22.8% N_2, 6.6% C_2H_6. N_2, as an inert specie, does not contribute to the heating value of the fuel.

The methane LHV can be derived with[32]:

$$LHV_{CH_yO_x} = \frac{396000 + 101600y - \frac{x}{1+y/2}(113600 + 101600y)}{12 + y + 16x} \tag{3.17}$$

It gives $LHV_{CH_4} = 50.150\ [MJ/kg]$, confirmed by [33]. The ethane LHV worth[34]: $LHV_{C_2H_6} = 47.8\ [MJ/kg]$. Therefore, the fuel mixture LHV is:

$$LHV_{fuel} = 70.6\% \cdot 50.150 + 22.8\% \cdot 0 + 6.6\% \cdot 47.8 = 38.56\ [MJ/kg]$$

Eq. 3.16 provides the primary power expression, it gives:

$$Wedge\ primary\ power\ = 2.853 \cdot 10^{-6} \cdot 38.56 \cdot 10^{6} = 110\ [W]$$

$$Burner\ primary\ power\ = 110.01 \cdot \frac{360}{5} = 7.920\ [kW]$$

The post-processing utility Paraview allows to extract the values of $\dot{Q}$ in the internalField (expressed in cell volume [W/m^3]). The heat released rate is also an extensive variable and requires a weighted sum to take the different contribution of the cells. Eq. 3.16 becomes:

$$\eta_{comb} = \left(\frac{\sum \dot{Q}_{cell} \cdot V_{cell}}{\dot{m}_{fuel}} \right)_{wedge} \cdot \frac{1}{LHV_{fuel}} \tag{3.18}$$

However, high value of η_{comb} could not be reached as the burner is only partially investigated. It is also believed that the configuration of the DJHC experiment providing the non-uniform data was not made for efficiency but only for the flame reproduction. As order of magnitude, the combustion efficiency was not higher than 5.5% for the adjusted simulation.

2. **Fuel consumption**
   The fuel consumption evaluation brings another perspective on the energy released during the combustion process. The fuel ratio here computed indicates the proportion of fuel remaining in the burner after the combustion. It corresponds to the ratio between the mass of hydrocarbons at the outlet and at the inlet:

$$FuelRatio = \frac{(\sum Y_{CH4,cell} \cdot M_{CH4} + \sum Y_{C2H6,cell} \cdot M_{C2H6})_{outlet}}{(\sum Y_{CH4,cell} \cdot M_{CH4} + \sum Y_{C2H6,cell} \cdot M_{C2H6})_{inlet}} \tag{3.19}$$

Table 2.6 provides the hydrocarbons mass fraction at the inlet. For the outlet, the *foamToVTK* command needs to be applied in the case terminal. Then, with Paraview, the hydrocarbons outlet mass fraction for each cell is extracted. Unlike $\dot{Q}$, a weighted sum is not performed here. It is due to the units of the mass fractions [-] which are not expressed in terms of cell surface.

3. **Maximal temperature**
As it is the hot spot of the flame where the main pollutants are generated, the variations of T_{max} are a concern. CO and NOx both increase quickly with the temperature (note that the detailed chemical mechanism used in the simulation does not contain the complex reaction mechanism of NOx). MILD combustion is also characterised by a distributed reaction zone. Therefore, the emergence of a significant temperature peak is unwanted.

$$T_{max} = max(T_{internalField}) \tag{3.20}$$

The values of the internalField are again obtained with Paraview.

4. **Flame width**
The window investigated does not allow to analyse variations of the flame height. Therefore, the focus is put on its width. The latter reflects the reactivity of the combustion, with the expansion of the flame width if the fuel needs more energy to react of if the availability of the oxidiser is less.
The flame corresponds to a thin layer. After a few tests, the radial cut at an axial position of 150 [mm] showed differences in maximal heat released position which then becomes the marker of flame width. The sampleDict post-processing utility in OpenFOAM provides the radial values of $\dot{Q}$ and by finding the maximal one, the corresponding radial position is retrieved.

3.3 Choice of uncertainties

The selection of the parameters to be investigated (also known as uncertainties) needs to be done carefully to alleviate the curse of dimensionality related to PCE (Eq. 3.5). They are chosen with regards to the outputs of interest but also to avoid correlated parameters. The selection involves two steps. At first, the so-called operational parameters have to be identified among the inputs set provided in Table 2.6. Then, the parameters of interest are chosen regarding some hypothesis and in order to avoid biased data.

3.3.1 Filtering: Operational parameters among inputs

The simulation contains 16 inputs in which species, thermodynamic as well as flow quantities are present. With a definition of what is meant behind the term *operational parameter*, most parameters can be dropped:

An operational parameter has a direct impact on the combustion and it can be independently modified from other quantities by an operator

- **Species:**
  The combustion products in the coflow can already be removed as they are related to reactions in the secondary burners. However, the coflow oxygen concentration can be adjusted through the air excess in these burners.
  The composition of the air can not be changed. The species left compose the fuel mixture. They translate the energy content of the fuel (LHV) and its value can be changed with a different composition (such as in Li. et al [17]). Therefore, the LHV (with the fuel composition) and the oxygen concentration in the coflow are held.

- **Thermodynamic quantities:**
  These inputs are: T, p, α_t, ν_t. The mean turbulent thermal diffusivity and kinematic viscosity are related to the fluid but also from different quantities developed in section 2.1.3. In theoretical conditions in which an air compressor could be added, the operating pressure of the combustion could be adapted. The same way, heat exchangers could modify the fluids mean temperature at the inlet.

- **Flow quantities:**
  These inputs are: k, ϵ, U. The mean turbulent kinetic energy dissipation rate ϵ is related to the mean turbulent kinetic energy through Eq. 2.53 and the latter is derived with the jet mean velocity (Eq. 2.54). In real-life applications, the mass flows can be adjusted and they control the jet velocities for a constant geometry and density. Note that the effects of pressure and temperature variations on the mass flows through the density are considered negligible compared to the jet mean velocities.

The filtering of the simulation inputs leads to obtain nine operational parameters: the operating pressure p, the fluids mean temperature (3x), the jet mean velocities (3x), the fuel LHV and oxygen mean mass fraction in the coflow.

3.3.2 Screening: Parameters of interest

Nine operational parameters implies an important number of evaluations for the PCE (Table 3.1) with regards to computational demand of the simulation. To alleviate this number, a second review on the previously selected parameters is performed. They are grouped by categories, namely the mean temperatures (with the operating pressure), the jet mean velocities (with the oxygen mean mass fraction in the coflow) and the LHV. The methodology lies in the making of assumptions and the identification of correlated parameters.

p	1	2
n	20	110

Table 3.1: Number of samples required to build the surrogate model for 9 uncertainties. Computed with Eq. 3.5.

- **Mean temperatures**

  1. Air:
  The assumption of an atmospheric burner is made, T_{air}= 293 [K] and **operating pressure** = 1 [bar] are then fixed for the study.

  2. Fuel:
  T_{fuel} is a key feature of MILD combustion. To make the combustion possible, it needs to reach a temperature above its self-ignition one (T_{ign}) in the reaction zone so that it can react spontaneously with the oxidiser. It is achieved through the heat transfer with the coflow jet. A variation of T_{fuel} should therefore impacts the ignition delay and consequently the fuel consumption.

  3. Coflow:
  T_{coflow} is another key feature of the regime as previously explained. Variations of T_{coflow} implies differences in the heat transfer and by acting directly on the fuel mean temperature, it impacts the ignition delay and fuel consumption. The preheat of the oxidiser also plays a role on the distribution of the reaction zone which decrease the peak temperature. Therefore, variations of T_{coflow} could also impact T_{max}.

- **Jet mean velocities**
  1. Air:
  The air flow acts as a buffer to prevent any stresses on the burner walls. It also feeds the coflow in oxygen. However, the air jet is not the first stream of oxidiser which the fuel meets and the feeding mechanism is not properly defined. Therefore the effects of U_{air} are not investigated in this work.

  2. Fuel:
  A variation of the fuel jet velocity implies a different amount of hydrocarbons mass entering the burner. It would then be impossible to evaluate if the fuel consumption evolves with the quantity of hydrocarbons, or due to the effects of other operational parameters.

  3. Coflow:
  There is a correlation between the **oxygen mean mass fraction in the coflow** $Y_{O_2,coflow}$ and the mixing intensity brought by the jet mean velocity U_{coflow}. If this latter increases, turbulence increases but so does $Y_{O_2,coflow}$ as it is present at 7.6% in the exhaust gases of the secondary burners. Then, it would not be possible to assess if the fuel consumption would be higher due to greater mixing or greater oxygen concentration. It is therefore necessary to understand the effect of leaner and richer environment on the combustion before having a look at the jet velocity of the coflow.

- **Fuel LHV**
  As mentioned in the previous section, different compositions of the fuel exist. It involves variations in the primary power which is interesting for combustion but it involves differences in the species mass fraction at the inlet which would bias the markers data. Then, the LHV remains constant for the present study.

The screening allows to end up with only three operational parameters to investigate: the oxygen mean mass fraction in the coflow, the coflow and the fuel mean temperatures. It brings a gain of 60% in terms of needed evaluations for the first polynomial order of the PCE:

p	1	2
n	8	20

Table 3.2: Number of samples required to build the surrogate model for 3 uncertainties. Computed with Eq. 3.5.

3.4 Ranges and sampling

The uncertain interval (stochastic space) around the reference value (design space, provided by Table 2.6) have to be defined. Only then, the samples can be generated according the a Sobol sequence with RHEIA. However, it is common to have a gap between theory and practice. The definition of the ranges makes no exception to this rule and tests need to be performed to ensure the validity of the intervals.

3.4.1 Theoritical intervals

$Y_{O_2,coflow}$ - Design value: 7.6%
The work of Perpignan et al.[3] provides a summary of the experiments made in JHC burners. The coflow oxygen concentration goes from 3% up to 15%, depending on the burner type. From the work of Oldenhof et al.[7], a maximal concentration of 10.9% is tested for a DJHC burner. Considering this value as the upper bound of the interval, it results the lower bound: 4.3%.
As $\sum Y_i = 1$ needs to be respected, the mean mass fraction of $Y_{N_2,coflow}$ is changed with regards to $Y_{O_2,coflow}$. It is assumed that this change has negligible impacts on the solution.

T_{coflow} - Design value: 1358 [K]
With regards to the same works of Perpignan et al., a maximal temperature of 1540 [K] is tested for a DJHC. The upper bound seems sufficiently high to induce a significant difference in the heat transfer. The lower bound is then 1176 [K].

T_{fuel} - Design value: 566 [K]
Unfortunately, no data about fuel temperature variations could be found. Therefore, the interval definition relies on different data and interpretations. The auto-ignition temperature of ethane and methane are respectively 808 and 873 [K][35]. The auto-ignition temperature of a mixture corresponds to the lowest auto-ignition temperature among the mixture species, here 808 [K]. A variation of 20% appeared as an admissible range. Indeed, this interval keeps a safety margin as an auto-ignition right at the fuel inlet pipe is not wanted. It gives a maximum temperature of 679 [K] which remains in the non-uniform values of the fuel temperature present in the initial simulation.

Table 3.3 summarises the discussion here above.

Uncertainty	Design space	Stochastic space	Interval
$Y_{O_2,coflow}$	7.6%	±3.3%	[4.3 ; 10.9] %
T_{coflow}	1358 [K]	±13.4%	[1176 ; 1540] [K]
T_{fuel}	566 [K]	±20%	[453 ; 679] [K]

Table 3.3: Uncertainties design and theoretical stochastic spaces.

3.4.2 Tests and final intervals

It is necessary to test the simulation under the maximal bounds of the intervals, individually and combined, to ensure that the simulation can carry the different uncertainties combinations. These tests are launched from the 43 000^{th} interval field of the simulation with the uniform boundary conditions. At first, only the upper bounds were investigated independently for 2000 intervals. Directly, two distinct behaviours arose for the two uncertainty types.

1. **Mean temperatures**
   The simulations with fuel and coflow maximal temperatures did not go to the end. The error message returned a division by zero, without more details on the cause. A too high disturbance induced by the upper values was pointed out as a possible origin of the error. Therefore, several values of the temperatures were tested to evaluate the simulation response (Table 3.4).

T_{fuel} [K]					
679	635	600	580	570	/
T_{coflow} [K]					
1540	1485	1420	1385	1375	1370

Table 3.4: Mean temperatures testing set.

   Unfortunately, the same error message appeared for all tests. This observation led to investigate the role of the relaxation factors in the PIMPLE algorithm. It aimed at reducing the pressure residuals which, by their relatively high but still admissible values (1e-2), could interfere in the solution by propagating a too large error when combined with an uncertainty disturbance. The relaxation factors limit the variable change from an iteration to the other. A factor of 0.5[1] has been imposed on every variable. It decreased the oscillations but they were still around 1e-2 and the simulations still crashed.

[1] On a scale from 1 to 0. 1 means no relaxation.

Other tests aimed at reducing the tolerances in the tabulation and reduction modules of TDAC to obtain more accurate results in the chemistry. Initially at 1e-4, they were both set to 1e-5 (independently first, combined then). Only a few more intervals could be achieved before the simulation crashed again.

The computational cost of the simulation does not allow to investigate all possibilities in due time. From the previous observations and the ones in section 2.2.3, the origin of the issue seems to be related to the solver algorithm. An improvement path should be privileged[36]:

- Relaxation factors: it is possible to assign a different factor value for each quantity. For example, the mean velocity reaches values under 1e-3, with weaker oscillations than the pressure. It could therefore require less relaxation. With 16 inputs, there exist multiple combinations and more tests need to be done.

2. **Oxidiser concentration**
Unlike the temperatures, the upper bound of the oxygen mean mass fraction in the coflow converged. However, with the observation for the mean temperatures, other values from the upper interval bound were tested (Table 3.5). Fortunately, the whole set converged and tests on the lower bound interval gave the same result.

$Y_{O_2,coflow}$ [%]			
10.9	9.8	9.1	8.2

Table 3.5: $Y_{O_2,coflow}$ testing set.

In the current state of the simulation, to perform an uncertainty quantification through a sampling-based PCE method is not practicable on the temperatures. Appendix C shows the first order Sobol sequence which would have been obtained with the initial bounds of Table 3.3. Nonetheless, with working simulations under oxygen concentration variations, their effects on the markers can still be evaluated and they are presented in the next chapter.

3.5 Summary

With non-uniform values ensuing from a non-optimised experiment and with only a window of the burner investigated, a poor combustion efficiency was observed, which does not reflect the possibilities of the regime. Other markers such as the fuel ratio, the maximal temperature and the flame width were therefore developed to capture the physics of the combustion.

Three non-correlated operational parameters ($Y_{O_2,coflow}$, T_{coflow}, T_{fuel}) were chosen among the inputs of the simulation to study their effects on the four markers. After the definition of their stochastic space, tests were performed to ensure that the simulation could carry out the extreme values of these intervals. It results that only the oxygen mean mass fraction in the coflow can be modified. The mean temperatures variations led the simulation to crash which needs further investigations to understand the error origin. Still, an analysis of $Y_{O_2,coflow}$ effects on the markers is possible.

Chapter 4

Results

The results hereafter describe the effects of the variations in $Y_{O_2,coflow}$ on the combustion markers. An interval of $\pm 2.2\%$ around the design value (7.6%) is considered. The outcomes are retrieved in Table 4.1.

$Y_{O_2,coflow}$ [%]	5.4	7.6	9.8
η_{comb} [%]	3.1	5.44	7.18
Fuel ratio [%]	65.1	64.65	64.52
T_{max} [K]	1391	1432	1432
Flame half-width [mm]	19	18	17

Table 4.1: Results on the markers for a variation of $\pm$ 2.2% in the coflow oxygen concentration $Y_{O_2,coflow}$.

From Perpignan et al.[3], the usual coflow oxygen concentrations for a DJHC burner are 7.6% to 10.9%. Therefore, the reduction of $Y_{O_2,coflow}$ show an expected decrease of fuel consumption. It translates less heat released, which results in a lower combustion efficiency. The mean temperature peak is also reduced.
However, despite that the upper bound has approximately the same amount of fuel consumed, a higher efficiency emerged for $Y_{O_2,coflow} = 9.8\%$ but without increasing the mean temperature peak. An evolution of the flame width is also noticed, becoming sharper with more oxygen.

To obtain a clearer view on these observations, the $Y_{O_2,coflow}$ values tested in Table 3.5 are used. The markers results are presented in Fig. 4.1.

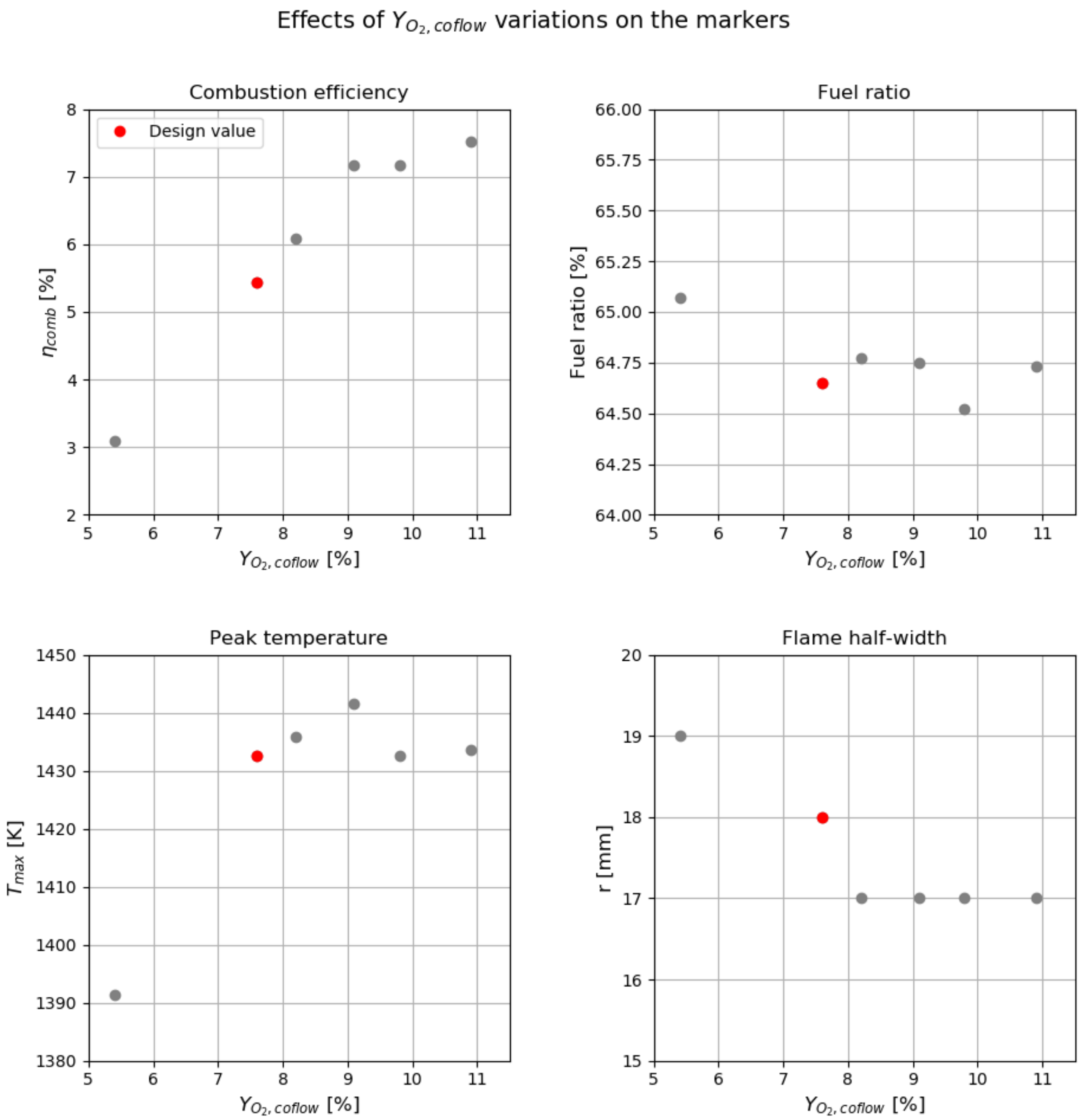

Figure 4.1: Effects of $Y_{O_2,coflow}$ variations on the different markers. Uniform boundary conditions. 2^{nd} adjustment of EDC coefficients.

From these graphs, the same conclusions as before can be drawn. The combustion efficiency increases with the coflow oxygen concentration. Still, the fuel consumption and temperature peak stay relatively the same for $Y_{O_2,coflow} \geq 7.6\%$. Passed the latter value, the flame width does not decrease more either.

A higher combustion efficiency for a fixed primary power reflects a higher amount of heat released. However, the stable fuel consumption indicates that the oxidiser reacts with other species. It increases therefore the quality of the combustion by extracting more heat from the fuel.
These reactions do not occur in a kernel but seem to be distributed as the temperature peak varies in a small range. Also, by increasing the availability of the oxidiser, the ignition starts earlier which results in a sharper flame and higher temperature peak upstream (Fig. 4.2). However, the fuel needs to reach its self-ignition temperature through heat transfer. Without modifications of T_{coflow}, the flame width seems to reach a plateau.

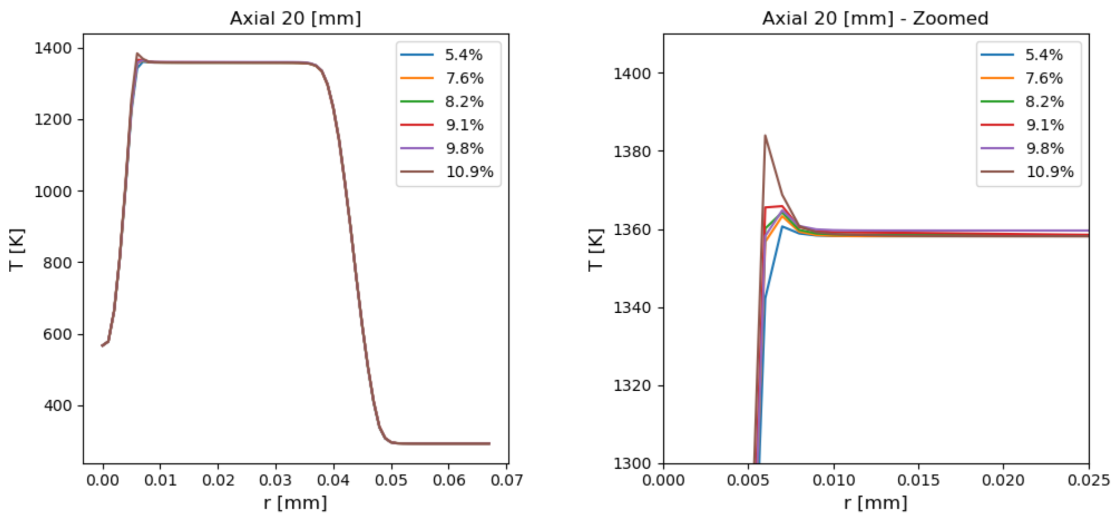

Figure 4.2: Upstream temperature profiles evolution with variations in $Y_{O_2,coflow}$ (left). Zoom on the temperature peak (right). Uniform boundary conditions. 2^{nd} adjustment of EDC coefficients.

These observations express a certain stability of MILD combustion with the increase of coflow oxygen concentration. This behaviour is wanted and shows the flexibility of the regime. The downstream temperature profiles in Fig.4.3 illustrate this characteristic, without significant change of those. On top of that, an addition of 3.3% to the $Y_{O_2,coflow}$ design value brought an increase of $\approx 2\%$ in combustion efficiency, without impacting the markers other than the flame width.

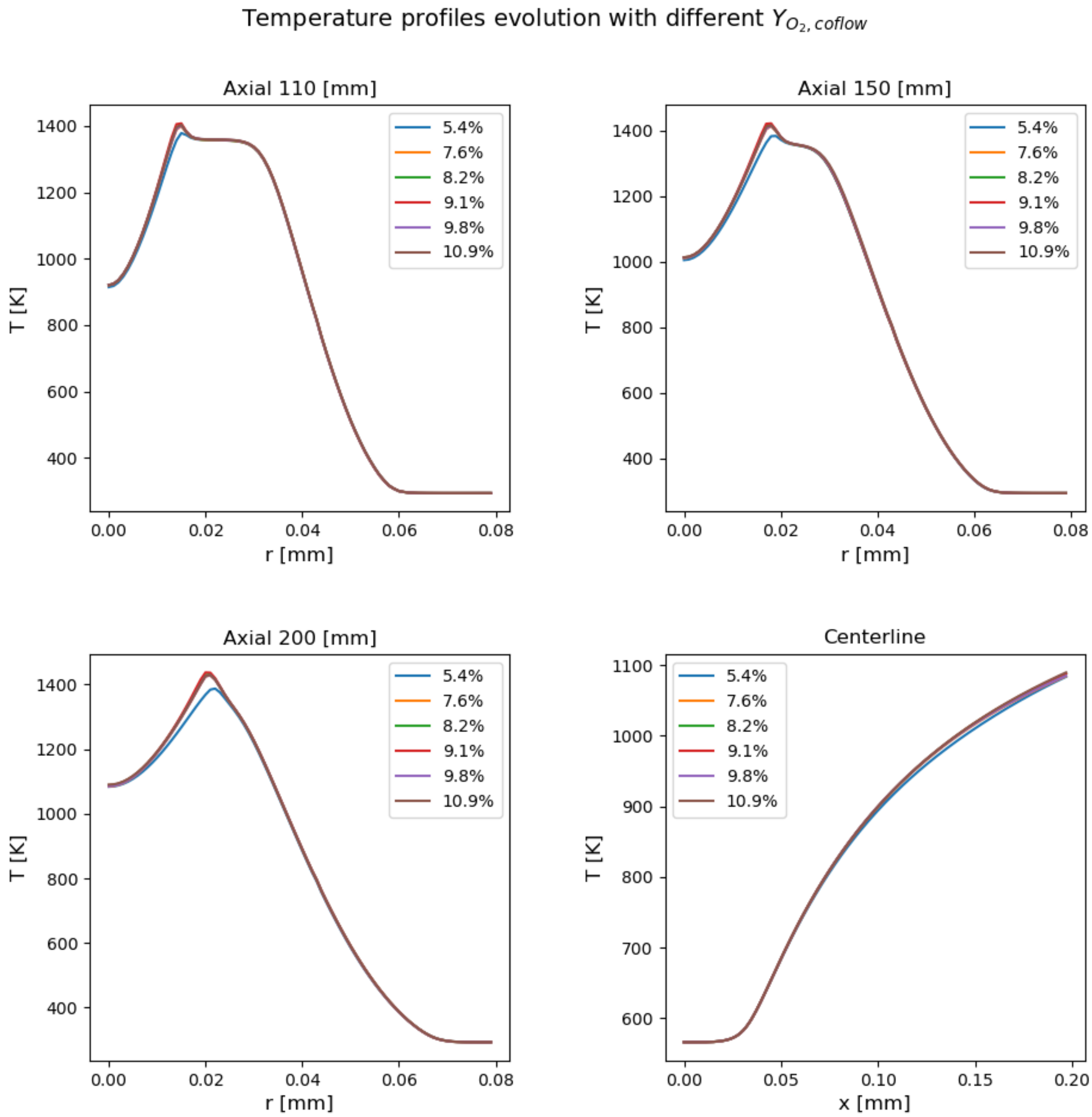

Figure 4.3: Downstream temperature profiles evolution with variations in $Y_{O_2,coflow}$. Uniform boundary conditions. 2^{nd} adjustment of EDC coefficients.

Chapter 5

Conclusion

A DJHC burner was numerically investigated in this work. The RANS approach models the turbulence while the DRM19 detailed chemical mechanism is used for finite rate chemistry. The objective of the study aims at defining the operational parameters of the simulation affecting different combustion markers, to better capture the physical process behind MILD combustion.

Initially, the investigation would have been achieved through a non-intrusive Polynomial Chaos Expansion which implies a change in the boundary conditions. Their switch to uniform gave satisfactory results in terms of heat transfer, fluid dynamics and flame structure. Also, the temperature over-prediction was decreased with an adjustment of the EDC2005 model coefficients. However, the simulation can not afford modifications of its thermodynamic quantities which limits the possibilities of the study. The analysis through PCE had to be dropped.

Nonetheless, the effects of the oxygen concentration in the coflow could be measured. While a reduction in the oxidiser availability showed expected results, an increase of its concentration highlighted the flexibility of MILD combustion. With the rising of the concentration, an improvement of the combustion efficiency was observed and this, without increasing the peak temperature nor the fuel consumption. The flame became sharper and the ignition started earlier. It results in a better conversion of the fuel within a distributed reaction zone.

The simulation needs improvements of its algorithm in order to pretend to a non-intrusive Polynomial Chaos Expansion analysis with regards to thermodynamic quantities. However, with a behaviour corresponding to MILD combustion, the simulation represents a work basis for further studies. To extend the present work, coflow oxygen mean mass fraction values exceeding the upper bound of the working interval should be investigated.

Appendix A

OpenFOAM case structure

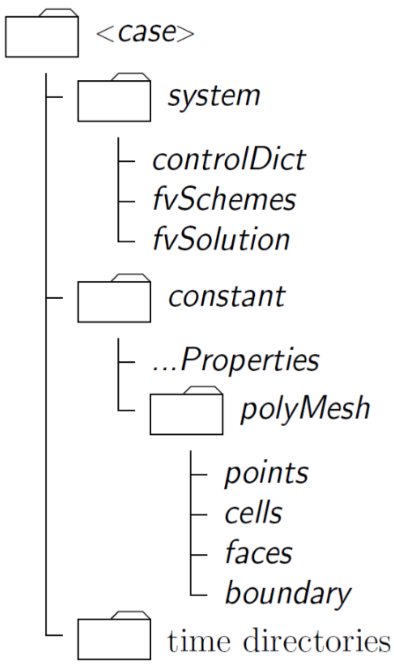

An OpenFOAM case corresponds to a files system, no graphical interface is at disposal. It contains at least 3 necessary folders: time, system and constant.

The **time** directories gather the boundary conditions of the case. To start, the simulation requires an initial time folder for which all the necessary inputs (species mass fraction, T, p, flow quantities) are specified by the user, for the internal field and each boundary of the domain. While the simulation is running, other time directories corresponding to defined interval can be created. This way, their boundary conditions and internal field are saved, and the user is not compelled to start from the beginning for every simulation if it is not necessary. This possibility is controlled in the *system/controlDict* file.

The **system** directory contains the files (at least the three mentioned on the picture) controlling the solution. *controlDict* gathers the control parameters of the simulation (among the start and end time, interval, results writing properties). *fvSchemes* specifies the discretisation schemes while *fvSolution* describes the equation solvers and algorithm control settings.

Finally, the **constant** directory contains the files describing both the case mesh in details (polyMesh) and the physical properties (e.g. the models of combustion, turbulence, chemistry).

Appendix B

Non-uniform boundary conditions weighted average results

```
################################################
This file contains the mean values of non-uniform BC for every parameters in the folder 0.
There are different fields:
internalField
boundaryField with FUEL,COFLOW, AIR, AXIS, TOP, OUTLET

If the field is not represented in the parameter-dict hereafter, it means it could be set to
uniform or the type does not include any value. No needs to be changed.
################################################


alphat
internalField : 0.00025691348427902286
FUEL : 0.00010786329860112799
COFLOW : 0.00010672781451660256
AIR :0.00011777215935537176
OUTLET :0.0007577718811581073

epsilon
internalField : 117.46159470177895
FUEL : 32561.387247112245
COFLOW : 0.3976882057526166
TOP: 0.05497461270695978
OUTLET :31.75952840811053

CH4
internalField : 0.006118855480956607

CH3O
internalField : 4.590401212184861e-09
```

```
H2
internalField : 1.7391607259602504e-05

H2O
internalField : 0.022693234866130514

T
internalField : 594.7442397479276
FUEL : 566.1572782629698
COFLOW : 1358.2411141637508
OUTLET :916.0403626626353

k
internalField : 0.31152030745828857
FUEL : 7.1954090508773065
COFLOW : 0.00678754602878848
TOP: 0.0027935559857479864
OUTLET :0.6963431185685324

C2H4
internalField : 1.3682343112822536e-05

N2
internalField : 0.7733549572864924

AR

cpu::reaction_times

HO2
internalField : 1.7615602232749823e-07

CO2
internalField : 0.026251980229545994

PaSR:kappa

O
internalField : 8.25526333610479e-06

Qdot
internalField : 304048.3250950036

one_over_tauStar

CH3
internalField : 6.06402040873037e-07
```

```
H
internalField : 1.3916361944585787e-06

CH2
internalField : 8.218711428605228e-10

HCO
internalField : 9.90434395223769e-10

drg::important_reactions

nut
internalField : 0.00025691348427902286
FUEL : 0.00010786329860112799
COFLOW : 0.00010672781451660256
AIR :0.00011777215935537176
OUTLET :0.0007577718811581073

C2H5
internalField : 1.1084405429113037e-08

CH2(S)
internalField : 3.967947937050156e-11

CH2O
internalField : 2.2497038603733597e-06

phi
internalField : 9.97920202510201e-07
FUEL : -2.853069992627849e-07
COFLOW : -1.6038814847000668e-06
AIR :-6.354441290691422e-06
OUTLET :3.0505005350722394e-06
back : -6.340631543442102e-18
front : 6.115230057193632e-18

p
internalField : 100001.41856714152

U
internalField : (1.6411337911295534; -0.05347361650876938; -1.3807992441758352e-13)
FUEL : (22.575316053689793; 0.0; 0.0)
COFLOW : (3.501900792890017; 0.0; 0.0)

dQ
internalField : 0.0006807229861030917
```

```
rho
internalField : 0.8363793959238346
FUEL : 0.39934396399635985
COFLOW : 0.2537059233357181
AIR :1.180820348738474
TOP: 1.1525867022792504
OUTLET :0.5161406825959969

O2
internalField : 0.17047162843907956

C2H6
internalField : 0.0005710890430861685

OH
internalField : 9.639875662940954e-05

CO
internalField : 0.0003980852594628149

drg::important_species
```

Appendix C

Sampling for polynomial order one

The samples are generated with the RHEIA framework according to a Sobol sequence. The design and stochastic space are gathered in Table 3.3.

Sample	T_{fuel} [K]	T_{fuel} [K]	$Y_{O_2,coflow}$ [%]
1	457.223	1364.80	5.597
2	458.988	1242.520	9.422
3	571.988	1424.520	6.122
4	628.488	1333.520	4.472
5	515.488	1515.520	7.772
6	543.738	1288.020	6.947
7	656.738	1470.020	10.247
8	600.238	1197.020	8.597

Table C.1: Samples generated by the RHEIA framework.

Bibliography

[1] Energy efficiency targets. https://ec.europa.eu/energy/topics/energy-efficiency/targets-directive-and-rules/eu-targets-energy-efficiency_en, October 2014.

[2] Nextmgt. https://nextmgt.com/.

[3] André A.V. Perpignan, Arvind Gangoli Rao, and Dirk J.E.M. Roekaerts. Flameless combustion and its potential towards gas turbines. *Progress in Energy and Combustion Science*, 69:28–62, November 2018.

[4] A.F. Colorado, B.A. Herrera, and A.A. Amell. Performance of a Flameless combustion furnace using biogas and natural gas. *Bioresource Technology*, 101(7):2443–2449, April 2010.

[5] PengFei Li, JianChun Mi, B. B. Dally, FeiFei Wang, Lin Wang, ZhaoHui Liu, Sheng Chen, and ChuGuang Zheng. Progress and recent trend in MILD combustion. *Science China Technological Sciences*, 54(2):255–269, February 2011.

[6] Masashi Katsuki and Toshiaki Hasegawa. The science and technology of combustion in highly preheated air. *Symposium (International) on Combustion*, 27(2):3135–3146, January 1998.

[7] E. Oldenhof, M.J. Tummers, E.H. van Veen, and D.J.E.M. Roekaerts. Role of entrainment in the stabilisation of jet-in-hot-coflow flames. *Combustion and Flame*, 158(8):1553–1563, August 2011.

[8] C Galletti, A Parente, and L Tognotti. Numerical and experimental investigation of a mild combustion burner. *Combustion and Flame*, 151(4):649–664, December 2007.

[9] S. Abraham. Uncertainty quantification in industrial turbo-machinery design using sparse polynomial chaos expansions. January 2018.

[10] Serhat Hosder, Robert Walters, and Rafael Perez. A Non-Intrusive Polynomial Chaos Method For Uncertainty Propagation in CFD Simulations. In *44th AIAA Aerospace Sciences Meeting and Exhibit*, Reno, Nevada, January 2006. American Institute of Aeronautics and Astronautics.

[11] Bruno Sudret. Polynomial chaos expansions and stochastic finite element methods. In Jianye Ching Kok-Kwang Phoon, editor, *Risk and Reliability in Geotechnical Engineering*, pages 265–300. CRC Press, 2015.

[12] Zhiyi Li, Michał T. Lewandowski, Francesco Contino, and Alessandro Parente. Assessment of On-the-Fly Chemistry Reduction and Tabulation Approaches for the Simulation of Moderate or Intense Low-Oxygen Dilution Combustion. *Energy & Fuels*, 32(10):10121–10131, October 2018.

[13] Diederik Coppitters and Panagiotis Tsirikoglou. Rheia framework. https://rheia.readthedocs.io/en/latest/index.html.

[14] www.wolfdynamics.com/wiki/fvm_crash_intro.pdf.

[15] Chris Greenshields. OpenFOAM v8 User Guide: 5.2 Boundaries. https://cfd.direct/openfoam/user-guide/v8-fvSchemes/x20-1450004.5, July 2020.

[16] Stephen B. Pope. *Turbulent flows.* Cambridge University Press, 2010.

[17] Zhiyi Li, Alberto Cuoci, Amsini Sadiki, and Alessandro Parente. Comprehensive numerical study of the Adelaide Jet in Hot-Coflow burner by means of RANS and detailed chemistry. *Energy*, 139:555–570, November 2017.

[18] Dobrin D. Toporov. Mathematical Modelling and Model Validations. In *Combustion of Pulverised Coal in a Mixture of Oxygen and Recycled Flue Gas*, pages 51–97. Elsevier, 2014.

[19] Changsi Chen, James J. Riley, and Patrick A. McMurtry. A study of Favre averaging in turbulent flows with chemical reaction. *Combustion and Flame*, 87(3-4):257–277, December 1991.

[20] B. E. Launder, G. J. Reece, and W. Rodi. Progress in the development of a Reynolds-stress turbulence closure. *Journal of Fluid Mechanics*, 68(3):537–566, April 1975.

[21] Amir Mardani. Optimization of the Eddy Dissipation Concept (EDC) model for turbulence-chemistry interactions under hot diluted combustion of CH4/H2. *Fuel*, 191:114–129, March 2017.

[22] Ashoke De, Ernst Oldenhof, Pratap Sathiah, and Dirk Roekaerts. Numerical Simulation of Delft-Jet-in-Hot-Coflow (DJHC) Flames Using the Eddy Dissipation Concept Model for Turbulence–Chemistry Interaction. *Flow, Turbulence and Combustion*, 87(4):537–567, December 2011.

[23] B. Magnussen. The eddy dissipation concept - a bridge between science and technology. *Invited paper at ECCOMAS Thematic Conference on Computational Combustion, Lisbon, June 21-24, 2005*, 2005.

[24] Francesco Contino, Jean-Baptiste Masurier, Fabrice Foucher, Tommaso Lucchini, Gianluca D'Errico, and Philippe Dagaut. CFD simulations using the TDAC method to model iso-octane combustion for a large range of ozone seeding and temperature conditions in a single cylinder HCCI engine. *Fuel*, 137:179–184, December 2014.

[25] Kun Wu, Francesco Contino, Wei Yao, and Xuejun Fan. On the application of tabulated dynamic adaptive chemistry in ethylene-fueled supersonic combustion. *Combustion and Flame*, 197:265–275, November 2018.

[26] Fluid Mechanics 101. [CFD] The PISO Algorithm. https://www.youtube.com/watch?v=ahdW5TKacok.

[27] Federico Municchi, Pranay P. Nagrani, and Ivan C. Christov. A two-fluid model for numerical simulation of shear-dominated suspension flows. *International Journal of Multiphase Flow*, 120:103079, November 2019.

[28] Chris Greenshields. OpenFOAM v8 User Guide: 5.2 Boundaries. https://cfd.direct/openfoam/user-guide/v8-boundaries/, July 2020.

[29] Javad Aminian, Chiara Galletti, Shahrokh Shahhosseini, and Leonardo Tognotti. Numerical Investigation of a MILD Combustion Burner: Analysis of Mixing Field, Chemical Kinetics and Turbulence-Chemistry Interaction. *Flow, Turbulence and Combustion*, 88(4):597–623, June 2012.

[30] https://code.kx.com/q/wp/option-pricing/.

[31] Dongbin Xiu and George Em Karniadakis. The Wiener–Askey Polynomial Chaos for Stochastic Differential Equations. *SIAM Journal on Scientific Computing*, 24(2):619–644, January 2002.

[32] H. Jeanmart. *Biomass Conversion.* Lecture slides.

[33] J. Martin D. Johnson and P. Wauters. *Thermal Power Plants – Energetic and exergetic approaches.* Presses Universitaires de Louvain-DUC, 2011.

[34] https://www.engineeringtoolbox.com/fuels-higher-calorific-values-d_169.html.

[35] https://www.engineeringtoolbox.com/fuels-ignition-temperatures-d_171.html.

[36] https://www.cfdsupport.com/Turbomachinery-CFD-manual/node65.html.

UNIVERSITÉ CATHOLIQUE DE LOUVAIN
École polytechnique de Louvain
Rue Archimède, 1 bte L6.11.01, 1348 Louvain-la-Neuve, Belgique | **www.uclouvain.be/epl**